Article

Mineralized collagen plywood contributes to bone autograft performance

https://doi.org/10.1038/s41586-024-08208-z

Received: 7 February 2023

Accepted: 11 October 2024

Published online: 20 November 2024

Open access

Check for updates

Marc Robin[1], Elodie Mouloungui[1], Gabriel Castillo Dali[2,10], Yan Wang[1], Jean-Louis Saffar[2], Graciela Pavon-Djavid[3], Thibaut Divoux[4], Sébastien Manneville[4,5], Luc Behr[6], Delphine Cardi[7], Laurence Choudat[8], Marie-Madeleine Giraud-Guille[1], Anne Meddahi-Pellé[3], Fannie Baudimont[9], Marie-Laure Colombier[2] & Nadine Nassif[1]✉

Autologous bone (AB) is the gold standard for bone-replacement surgeries[1], despite its limited availability and the need for an extra surgical site. Traditionally, competitive biomaterials for bone repair have focused on mimicking the mineral aspect of bone, as evidenced by the widespread clinical use of bioactive ceramics[2]. However, AB also exhibits hierarchical organic structures that might substantially affect bone regeneration. Here, using a range of cell-free biomimetic-collagen-based materials in murine and ovine bone-defect models, we demonstrate that a hierarchical hybrid microstructure—specifically, the twisted plywood pattern of collagen and its association with poorly crystallized bioapatite—favourably influences bone regeneration. Our study shows that the most structurally biomimetic material has the potential to stimulate bone growth, highlighting the pivotal role of physicochemical properties in supporting bone formation and offering promising prospects as a competitive bone-graft material.

The osteoconductive and osteoinductive properties[1,3] of AB are mainly attributed to its biological characteristics, that is, the presence of progenitor cells, osteoblasts and blood cells, fresh growth factors, pre-existing vascular network, extracellular matrix (ECM) composition including mineralized collagen and an inherent and total immunocompatibility[2]. Additionally, the physical properties of the substrate are now considered crucial for driving the physiological cells phenotype expression, opening a new paradigm for cell–matrix interactions and mechanobiology[4–9]. Such a structure–function relationship in bone is also fundamental[10,11]. Notably, the collagen–mineral composite structure determines the final properties of bone material, which does not solely depend on the mineral quantity, rather on the interactions between the organic and mineral components[12]. These cooperative mechanisms of deformation take place at different length scales, from the intrafibrillar to the tissue organizational level. Despite the recognized importance of microstructure hierarchy in fundamental research, its application in the development of competitive bone grafts tends to be overlooked, with the emphasis placed on achieving bone properties by means of mineral formulation (for example, bioceramics). The organic components in mineral-based scaffolds merely serve as a 'simple' coating to improve cell attachment[13]. However, demineralized bone is a self-standing material (Supplementary Video 1), whereas the mineral counterpart exists as a powder (Extended Data Fig. 1), highlighting the importance of the organic scaffold for bone mechanical properties. Another notable deviation is the degree of crystallization of these alternative materials (highly crystalline hydroxyapatite (HA) versus bioapatite). Various experimental methodologies are used to decipher both biological and mechanical aspects involved in this complex physiological process, increasingly supplemented by computational modelling[14]. However, synthetic bone materials still markedly differ from the native tissue, as they fail to integrate both the bone composition and its microstructure simultaneously.

Bone is characterized by a hierarchical organization, usually categorized into distinct structural levels[10,15]. It is a hybrid material, mainly composed of type I collagen fibrils and poorly crystalline apatite nanoparticles. In both compact (Fig. 1a) and trabecular bone tissues, the elongated orientation of the apatite platelets tends to align preferentially along the long axis of the collagen fibrils. A notable characteristic is the presence of a twisted plywood pattern made of mineralized collagen fibrils[10,15,16] (Fig. 1b). Such a structural feature encompasses a high density of monodispersed collagen fibrils coupled with a high degree of structural order. The mineralized plywood was successfully reproduced in 3D scaffolds[17,18] by using the lyotropic properties of type I collagen in vitro[19], the co-alignment[20] being performed with biomimetic carbonated apatite. These materials combine the three main components of bone (collagen, apatite and water) providing, to the best of our knowledge, the highest level of in vitro bone organization achieved so far (that is, 9 out of 12 levels[15]). Consequently, these constructs present an opportunity for investigation as bone models to explore the importance of such structural characteristics in autologous graft performance, potentially paving the way for the development of a new type of competitive bone biomaterial.

Here we propose that the microstructure of bone is just as crucial as its molecular and cell biological components in determining the

[1]Laboratoire de Chimie de la Matière Condensée de Paris (LCMCP), Sorbonne Université, CNRS, Collège de France, Paris, France. [2]URP2496, Laboratoire Pathologies, Imagerie et Biothérapies Orofaciales, UFR d'Odontologie, Université Paris Cité, Montrouge, France. [3]Laboratory for Vascular Translational Science, Cardiovascular Bioengineering, Université Sorbonne Paris Nord, Inserm U1148, Villetaneuse, France. [4]Laboratoire de Physique, ENSL, CNRS, Lyon, France. [5]Institut Universitaire de France (IUF), Paris, France. [6]IMM Recherche, Paris, France. [7]SATT Lutech, Paris, France. [8]Département de Pathologie, Hôpital Bichat, Paris, France. [9]ABS Atlantic Bone Screen, Saint-Herblain, France. [10]Present address: Instituto de Ciencia de Materiales de Sevilla (ICMS), Consejo Superior de Investigaciones Científicas, Seville, Spain. ✉e-mail: nadine.nassif@sorbonne-universite.fr

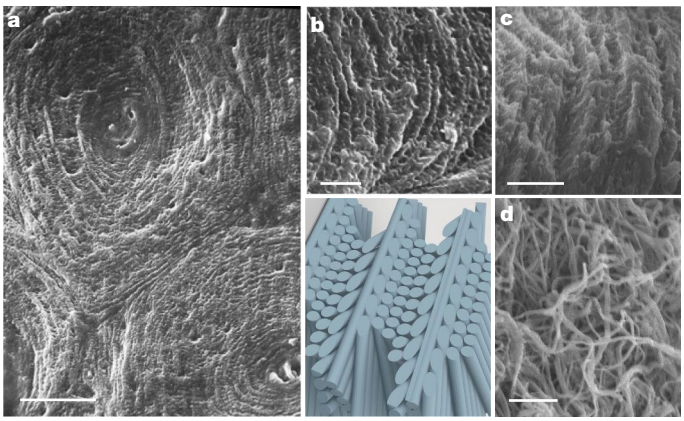

Fig. 1 | Characterization of collagen suprafibrillar organization in bone and synthetic collagen-based materials. a,**b**, SEM micrographs of decalcified human compact bone (n = 1 sample) at low and high magnification, respectively. Scale bars, 50 µm (**a**), 5 µm (**b**). **c**, SEM micrograph of synthetic collagen-based materials characterized by a 3D dense and organized biomimetic structure (Col100; n = 3 samples). Scale bar, 5 µm. The plywood organization is depicted in the associated schematic representation below **b**. **d**, SEM micrograph of a non-organized collagen fibrillar network with large (micrometric) interfibrillar spaces (Col40; n = 3 samples). Scale bar, 2 µm.

healing efficacy of AB. Accordingly, we present findings on how the bone hierarchical microstructure, specifically the collagen plywood and the related bioapatite co-alignment, contributes to bone regeneration in rat and ewe bone defects[21] using a variety of tuned cell-free biomimetic scaffolds. Then, their capacity to enhance bone growth was compared with commercially available synthetic ceramics and the established AB gold standard.

Collagen plywood promotes rat bone healing

Although murine bone lacks the osteon units[22,23] found in human bone, which consist of concentric layers of collagen fibrils with successive different orientations[16], it still showcases successive dense fibrillar layers with differing orientations, akin to those observed in human bone (Extended Data Fig. 2a).

We evaluated dense collagen matrices containing two variations (see Methods): one comprising twisted plywood of fibrils (100 mg ml^{-1}; Col100) and another with randomly dispersed fibrils (40 mg ml^{-1}; Col40), as shown by scanning electron microscopy (SEM) (Fig. 1c,d, respectively).

A rat calvaria critical-size defect (Fig. 2a) was created[24,25] (Extended Data Fig. 2b–d). Briefly, a piece of cranial bone (Fig. 2b) was extracted and the defect either filled with the collagen-based matrices (Col40 (n = 10) and Col100 (n = 10)) (Fig. 2c and Extended Data Fig. 2b) or left empty to serve as a control (n = 8). Notably, the implants immediately adhered to bone and dura mater (Extended Data Fig. 2c). This contact is crucial for bone repair and is potentially facilitated by the well-known haemostatic properties of collagen. Microradiographs were used to estimate the area covered by newly formed mineralized tissue, expressed as a percentage of bone defect closure (Extended Data Fig. 3).

In the control group, bone-growth pattern was centripetal, processing inward from the defect rim (Fig. 2d1,e1) with a very small amount of newly formed bone after 10 weeks (15.2 ± 9.0%). However, in the cases in which defects were filled, there was a significant increase in the mean percentage of bone-defect reconstruction, reaching 69.2 ± 24.1% for Col40 (Fig. 2d2) and 87.9 ± 6.1% for Col100 (Fig. 2d3). Complete defect reconstruction was observed in 40% and 60% of animals with Col40 and Col100, respectively. Unlike the control group, microradiographs and micro-computed tomography (µCT) scans of explants from the implants groups revealed the formation of mineralized structures originating independently from the edges of the defect and growing from its core (Fig. 2d2,d3,e2,e3), as described earlier[26]. Despite the notable discrepancy in the average percentage of mineralized filling between Col40 and Col100, this difference lacks statistical significance, even if a trend emerges (P = 0.086). Notably, the biological response for Col40 shows considerable variability owing to some very low mineralized filling values observed for certain animals. By contrast, Col100 demonstrates improved reproducibility (with a s.d. of 6.1% compared with 24.1% for Col40) (Extended Data Fig. 3a). Notably, only 40% of the implant sites filled with Col40 show a binding between the defect edges and the host bone on at least half of the rim, whereas in animals implanted with the anisotropic Col100, it is found in approximately 70% of cases. Also, µCT observations of a defect implanted with Col40 show small and less radiopaque domains in the thickness of the new forming bone, indicating the presence of non-mineralized tissue (Fig. 2e2). By contrast, a more homogeneous and mature mineralized bone repair is observed for Col100 (Fig. 2e3).

The histological analysis (illustrated in Fig. 2f–h) confirms the formation of mineralized tissue, guided by the collagen matrices from the centre of the defect (Fig. 2f). No evidence of bone reconstruction is observed in the control (Fig. 2f1). However, for Col40, the observations show the presence of both mineralized domains and residual collagenic material (Fig. 2f2,g1,h1). This remnant material (Fig. 2g1,h1, yellow star) seems to undergo (1) 'in situ mineralization'[27] without apparent remodelling or ossification (Fig. 2g1,h1, yellow dot) and (2) angiogenesis with infiltration by many cells, either isolated or structured in blood vessels (Fig. 2g1, yellow and black arrows). These remaining material areas are surrounded by dense mineralized collagen zones showing active remodelling with resorption lacunae and deposition of osteoid tissue (active osteoblasts) organized around large vascular structure (Fig. 2g1, blue stars), characteristic of mature bone production (red dot). Notably, a lamellar bone formation is observed on the external surface of the matrix (Fig. 2h1, yellow circle), mostly at the exocranial aspect, demonstrating the osteoconductive properties of Col40.

The integration process for Col100 seems qualitatively similar. A mineralization of the implanted matrix (Fig. 2g2, yellow star) is observed without structural modifications (yellow dot), a phenomenon correlated with the presence of Ca and P ions (Extended Data Fig. 4). Concomitantly, endothelial cells infiltrate the matrix with sprouting small vessels (Fig. 2g2, yellow and black arrows). They provide 'on-site' bone remodelling cells possibly involved in the resulting mature bone (Fig. 2g2,h2, yellow cross) formed through remodelling (red dots) around vascularized spaces (blue stars). Similar to Col40, a lamellar bone formation on the external part of the matrix is found with Col100 (Extended Data Fig. 5a).

The key difference between Col40 and Col100 lies in the overall implant-scale bone formation. Indeed, Col100 exhibits a more homogenous bone formation within the defect thickness (Fig. 2f3). with widely mineralized domains (Fig. 2h2, cross). Furthermore, a notable surface area of the implant includes zones featuring small medullar spaces containing vessels and cells (Fig. 2h2, blue stars), accompanied by rows of active osteoblasts depositing osteoid matrix along mineralized bone trabeculae (red dots). The presence of bone-marrow spaces is considered beneficial for sustained healing by osteogenesis, as it serves as a vital source of nutriments and progenitor cells for bone tissue[28]. Moreover, the remodelling seems more intense in the newly formed bone with Col100 compared with Col40, as evidenced by alkaline phosphatase (ALP) and tartrate-resistant acid phosphatase (TRAP) enzyme histochemistry (Extended Data Fig. 5b,c). Indeed, lower resorption and osteoblasts recruitment activities are observed for Col40 (with an average of 4 osteoclasts mm^{-1} versus 7 osteoclasts mm^{-1} for Col100), explaining both the heterogeneous reconstruction observed in the radiographic analysis and the slightly weaker percentage of mineralized tissue surface extracted from von Kossa sections for Col40 compared

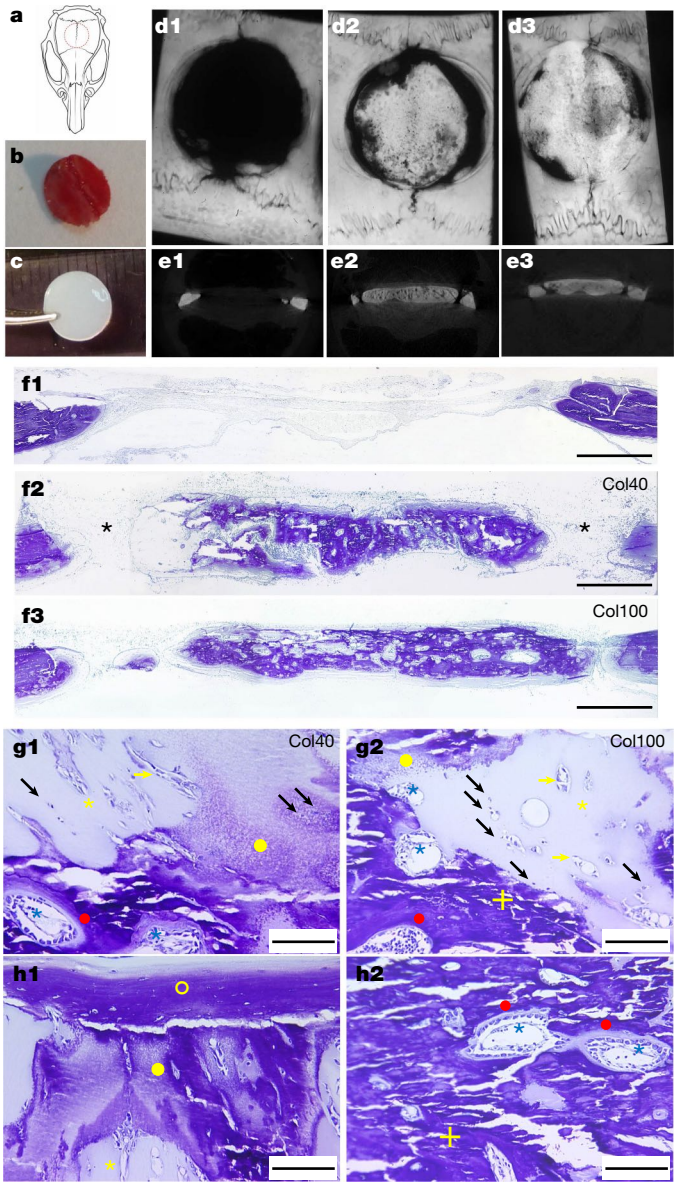

Fig. 2 | Effect of collagen-based matrices in calvaria bone-defect model. **a**, Schematic representation of rat calvaria showing the characteristics of the defect (localization, size and shape; dashed red circle). Pictures of the 8-mm-diameter removed cranial bone piece (**b**) and collagen matrix implant (Col40) (**c**). Representative microradiographies of the empty-site control (**d1**; $n = 6$ defects) and defect filled with Col40 (**d2**; $n = 10$ defects) and Col100 (**d3**; $n = 9$ defects). µCT scans of a representative control (**e1**) and defect filled with Col40 (**e2**) and Col100 (**e3**). Representative overview by toluidine-blue-stained histological sections of defect left empty (**f1**; $n = 6$ defects) or implanted with Col40 (**f2**; $n = 10$ defects) or Col100 (**f3**; $n = 9$ defects). Col40 is partly replaced by mineralized tissue surrounded by areas of unbound bone edges (stars). Conversely, bone formation in Col100 is more homogeneous and the bounding of bone edges is more frequent. Scale bars, 1 mm (**f1**, **f2**, **f3**). At higher magnification, both Col40 (**g1**) and Col100 (**g2**) matrices show a similar integration mechanism. Remnant matrix (yellow star) is observed infiltrated by vascular cells (isolated or structured in blood vessels, black and yellow arrows, respectively). Concomitantly, the remnant matrix is undergoing an in situ mineralization without structural changes (granular aspect and more intense staining, yellow dot). The remnant matrix areas are surrounded by more mature bone regions with areas of active osseous formation, including remodelling sites around medullar spaces (blue stars) and osteoid tissue deposition (red dots). For Col100, larger medullar structures are observed, leading to mature bone formation (yellow cross). **h1**, A newly formed lamellar bone containing osteocytes (yellow circle) that surrounds a less mature fraction of Col40 (yellow dot for mineralized areas and yellow star for remnant material). **h2**, For Col100, a more mature lamellar bone morphology (yellow cross) is observed, with noticeable marrow spaces (blue stars), containing vessels surrounded by osteoblasts forming osteoid matrix (red dots). Remnants of the collagen matrix are more sparsely distributed. Scale bars, 50 µm (**g1**, **g2**, **h1**, **h2**).

with Col100 (41.0 ± 9.1% versus 49.8 ± 13.9%; Extended Data Fig. 3b). These findings demonstrate that bone formation with Col40 is less pronounced than with Col100, indicating that the latter induces a more active bone reconstruction by comparison.

Several factors may contribute to the performance of the Col100 matrix, including: (1) enhanced mechanical properties associated with increased collagen concentration[29,30], leading to a notable 100-fold increase in the Young's modulus when compared with the Col40 as measured by microindentation, performed at the cell scale, that is, of about 10 µm (Supplementary Table 1 and Extended Data Fig. 6); (2) the new microenvironment set by the material composition, density and/or organization, probably favouring the migration of host cells and the correct expression of their phenotype[4,6,9]; and (3) a possible electrostatic environment created by the collagen fibrils density that is known to dictate mineralization in vitro[31]. Another important consideration is that bone healing begins with the formation of a collagenic scar tissue, gradually maturing with the production of dense collagen by osteoblasts originating from the surrounding bone and periosteum. The resulting tissue is then mineralized at a later stage[32]. The use of AB bypasses these steps by immediately providing an existing vascular network, potentially connecting to surrounding vessels as observed in pre-vascularized scaffolds[33]. Also, it provides the native microenvironment with respect to the quantity and quality of collagen fibrils, their organization and density, as well as other bone components, such as mineral, cells and growth factors. The bone-like twisted plywood in Col100 might similarly induce, to some extent, such a sequence of events.

Notably, Col100 is a bulk material with porosity at the nanometre scale, whereas Col40 exhibits larger interfibrillar spaces at the micrometre scale, averaging 10 µm in pore size[30] (Fig. 1c,d). Here, similar to AB graft and dense collagen matrix in vitro[34], the high fibrillar density and organization do not hinder cell migration. In fact, it seems to enhance cell migration compared with a matrix with lower collagen density. This suggests that the conventional notion in the literature favouring macroporous scaffold for cell colonization and subsequent bone healing might not be mandatory when mimicking the composition and microstructure of the ECM. Accordingly, local lamellar orientation and a continuous curvature have been shown to orient bone-tissue formation[9,35].

In summary, our findings indicate that the quality of bone reconstruction improves when the biomaterial replicates the plywood structure of the host native bone. Also, our results confirm that physicochemical properties take part in bone healing by driving the biological response. Considering the differences in tissue architecture between murine and human bone[22], further experiments were conducted using a preclinical ewe model. Indeed, sheep shares substantial similarities with human in weight, bone and joint structure and in bone regeneration[21].

Mineralized plywood enhances ewe bone repair

We investigated the addition of apatite mineral—specifically, biomimetic carbonated HA (CHA)—whose arrangement in collagen (that is, co-alignment, marked as a star in transmission electron microscopy (TEM)[20]; Fig. 3a), composition, size, hydration[36] and structure[37] (wide-angle X-ray diffraction (WAXD); Fig. 3b) closely resembles that found in bone[38] (Fig. 3c). Comparative mechanical analysis against a non-mineralized matrix exhibiting identical collagen plywood organization (Col) revealed that this hybrid material (Col-CHA) shows much

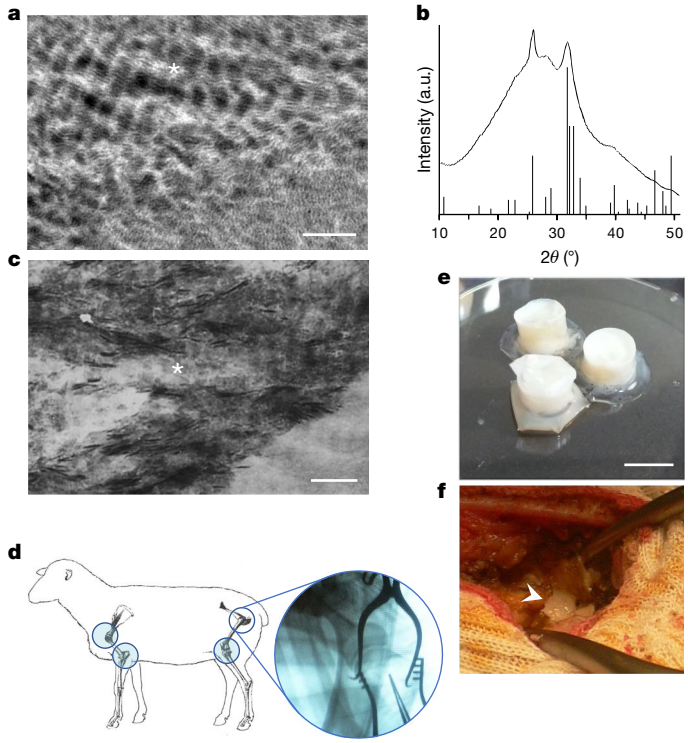

Fig. 3 | Characterization and implantation of bone-like material in ewe model. a, TEM micrograph of Col-CHA ($n = 3$ samples), in which the collagen–apatite co-alignment is observed (star). Scale bar, 500 nm. **b**, 1D radial average of the WAXD pattern of Col-CHA and the X-ray diffraction pattern of synthetic HA from the database PDF-5+ (JCPDS #00-009-0432). **c**, TEM micrograph of partially decalcified human compact bone (as shown in **a**; the typical co-alignment is highlighted by a star) ($n = 1$ sample). Scale bar, 500 nm. **d**, Schematic representation of the ewe surgical procedure and metaphyseal implantation sites (spherical inset). Pictures of Col-CHA (about 8 mm in diameter) before (**e**) and during (**f**) implantation, its size and shape fitting the bone defect (arrowhead). Scale bar, 1 cm. a.u., arbitrary units.

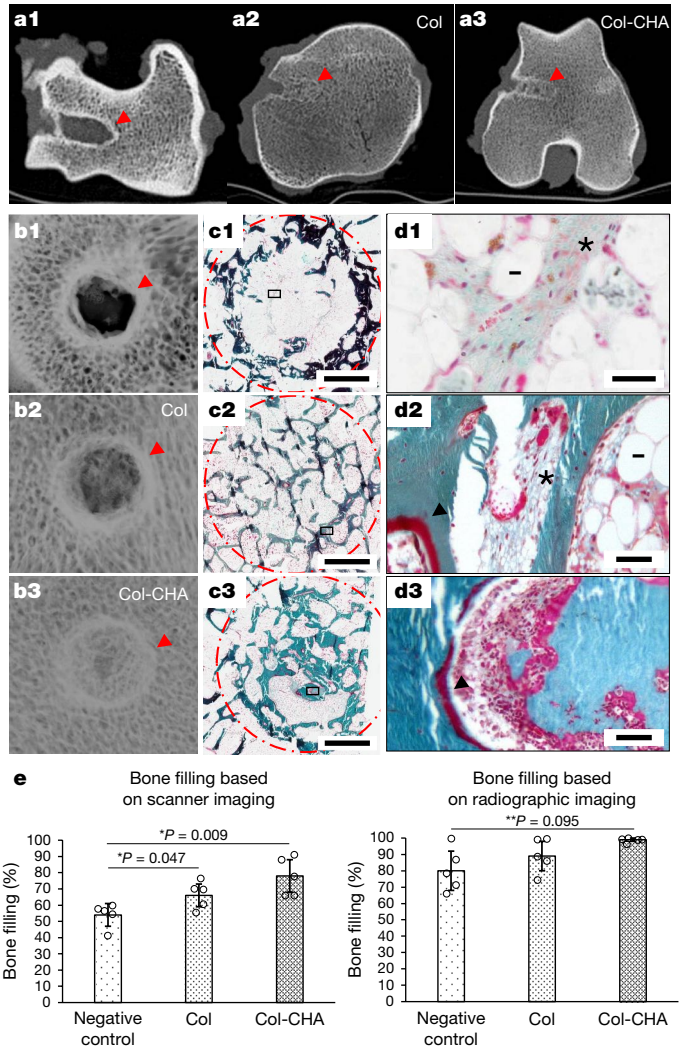

Fig. 4 | Comparison of bone materials in ewe model after 2 months of implantation using non-mineralized or mineralized twisted plywood scaffolds. Scanner imaging sections of the control in which the defect was left empty (**a1**; $n = 5$ defects), ewe implanted with Col (**a2**; $n = 5$ defects) and Col-CHA (**a3**; $n = 5$ defects) matrices. Red arrowheads show the original defect identified by strong peripheral ossification as a result of the surgical procedure. Faxitron radiographic imaging of the empty-site control (**b1**; $n = 5$ defects), ewe implanted with Col (**b2**; $n = 5$ defects) and Col-CHA (**b3**; $n = 5$ defects) matrices. The strong peripheral ossification is also evidenced here (red arrowheads). Histological GT-stained thin sections of implantation sites for the empty-site control (**c1**,**d1**; $n = 5$ defects), Col (**c2**,**d2**; $n = 5$ defects) and Col-CHA (**c3**,**d3**; $n = 5$ defects) matrices. Dashed-dotted red circles represent the approximate initial defects. Higher-magnification observations allow the visualization of tissular components and organization: fat adipose tissue (bars), collagenic scar tissue (stars) and bone trabeculae with remodelling (black arrowheads). Sections are perpendicular to the long axis of the defect. Scale bars, 2 mm (**c1**,**c2**,**c3**), 50 µm (**d1**,**d2**,**d3**). **e**, The percentage of bone filling for each defect was blindly measured on radiographies and scanner imaging. Data were analysed from the total number of defects in each group, as indicated in the bars ($n = 5$), expressed as mean ± s.d. and compared using nonparametric Kruskal–Wallis with Mann–Whitney multiple comparison test (scanner imaging) or independent unpaired two-sided Mann–Whitney tests (radiographic imaging). *Significant difference with $P < 0.05$. **A difference/trend with $P < 0.10$.

larger Young's moduli at the micrometre scale. Furthermore, the local Young's modulus shows a much broader distribution in Col-CHA, as previously reported[20] (Supplementary Table 1 and Extended Data Fig. 6).

Both Col and Col-CHA were surgically implanted into critical-size bone defects (cortico-cancellous sites) in ewes[39,40] (Fig. 3d) (see Methods). As for the previous implantations, the biomaterials were shaped to fill the defect (Fig. 3e) and then implanted (Fig. 3f; $n = 5$ for each matrix). After 2 months, bone blocks were scanned computed tomography (Fig. 4a), radiographed (Fig. 4b) and prepared for histopathological analysis (Fig. 4c,d). The sites of bone defects were easily detected thanks to the rim of adjacent bone (Fig. 4a,b, arrowheads), which is a consequence of the surgical procedure and subsequent inflammation. The area covered by bone was measured on both radiographic images and slices extracted from the scanning and were expressed as a percentage of bone formation (Fig. 4e). For the histological images, only the internal part of the explants is shown, excluding the strong and non-specific surface reaction owing to the mechanical load applied on the external part[41].

When the defects were left empty ($n = 5$) as controls (Fig. 4a1,b1), the percentage of newly formed mineralized bone was found to be 80 ± 12% on radiography and 54 ± 7% on scanner. This difference is attributed to the techniques used. Specifically, the frontal X-ray radiographic imaging method inherently stacks all depth levels into a single image, occulting potential reconstruction flaws inside the defect and consequently resulting in higher filling percentages. Conversely, the lateral scanner imaging technique enables the differentiation between superficial and internal bone reconstruction, thereby leading to lower filling percentages. Moreover, apart from the evident strong peripheral ossification that shows newly formed bone close to the defect border (Fig. 4c1, within the dashed-dotted red circle), the centre of

the unfilled defect exhibits fatty and collagenic scar tissues, as shown in the histopathological sections (Fig. 4d1, bar and star, respectively). These results indicate a minimal amount of newly formed bone, failing to recover both the native physiological and mechanical functions, as well as local morphology.

By contrast, the percentage of newly formed bone in the presence of Col exhibits substantial increase (89 ± 9% on radiography and 66 ± 7% scanner; Fig. 4a2,b2). Similar to the control group, all sites implanted with Col show a strong peripheral ossification (arrowheads), but not always evidenced in histopathological observations (Fig. 4c2, dashed-dotted red circle). However, as well as locally loose collagen aggregates in few areas (Fig. 4d2, star), the internal volume of the defect is mainly filled with newly formed lamellar bone composed of a bone trabeculae network and vascularized medullary spaces (Fig. 4d2, arrowhead and bar, respectively). The resulting network is connected with the surrounding trabecular system and reproduces the local architecture. This newly formed bone seems morphologically normal, with areas of physiologic remodelling (Fig. 4d2, red osteoid layer, arrowhead), albeit with fewer interconnections compared with the surrounding bone. The presence of deep-seated reconstruction within the defect distinguishes it markedly from the control, as observed in scanner imaging (Fig. 4a2).

Addition of biomimetic co-aligned CHA to Col results in a further increase of new bone formation (99 ± 1% on radiography and 78 ± 10% on scanner; very different compared with the control; Fig. 4a3,b3). The high degree of bone reconstruction inside the defect shows the limitation of the radiographic evaluation. Notably, the peripheral ossification is less visible and the reconstruction is localized within the whole defect volume. Furthermore, the bone trabeculae seem thicker, with increased interconnections compared with those observed with Col alone. This trend suggests a higher bone density, consistent with both radiographic imaging and histopathological observations (Fig. 4c3,d3). Despite the rapid bone reconstruction, the local architecture seems physiological, featuring vascularized medullary spaces between trabeculae and normal bone remodelling sites (Fig. 4d3, arrowhead).

These results confirm, in a more challenging bone-healing model, that the collagen plywood greatly enhances bone reconstruction compared with self-healing (control). Furthermore, the biomimetic mineralization of this hierarchical collagen structure improves the healing process. This outcome is in line with previous in vitro studies that illustrate the influence of collagen–apatite co-alignment on osteoblasts reaction and mobility[34]. It is well known that addition of calcium phosphate to collagen scaffold stimulates bone healing[42]. Furthermore, apatite deposition aligned along the long axis of the collagen fibrils has been linked to superior bone reconstruction compared with isotropic mineralization around the fibrils[43]. However, this effect has not previously been demonstrated for hierarchically organized co-aligned collagen–apatite, specifically depicting the twisted plywood geometry. Note that further studies may determine whether an optimum collagen–apatite composition exists.

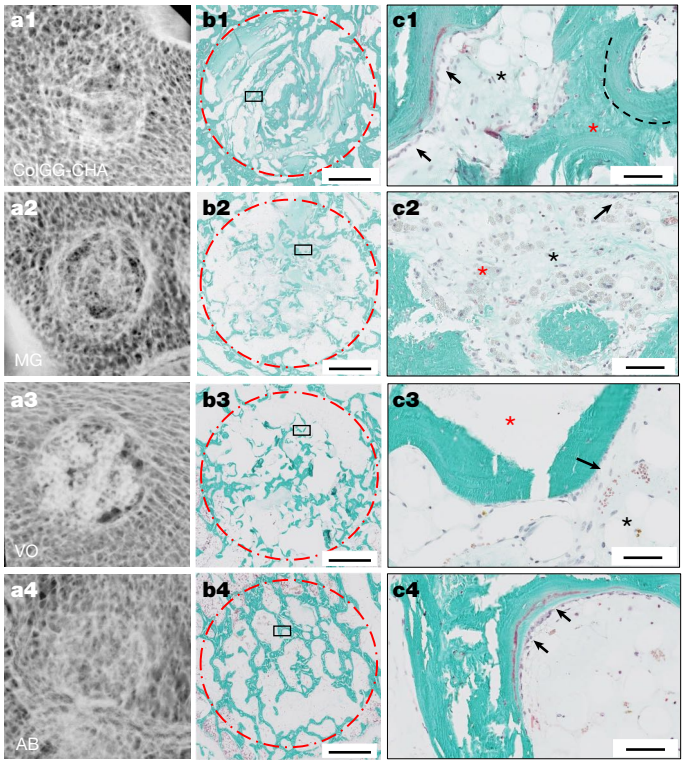

Fig. 5 | Comparison of bone formation in ewe model between bone-like material, ceramic biomaterials and AB after 2 months of implantation. Faxitron radiographic imaging of ewe bone defects implanted with ColCG-CHA matrices (**a1**; $n = 12$ defects), MG ceramic (**a2**), VO ceramic (**a3**) and AB graft (**a4**) ($n = 5$ for MG, VO and AB). Histological GT-stained thin sections of ewe bone defects implanted with ColCG-CHA matrices (**b1**; $n = 12$ defects), MG ceramic (**b2**), VO ceramic (**b3**) and AB graft (**b4**) ($n = 5$ for MG, VO and AB). Dashed-dotted red circles represent the approximate initial defect. Scale bars, 2 mm. Higher-magnification observations (**c1**–**c4**, ColCG-CHA, VO, MG and AB, respectively) allow the visualization of tissular components and organization, such as residual materials (red stars in **c1** and **c2**), active (black arrows in **c1** and **c4**) or quiescent osteoblast layers (black arrows in **c2** and **c3**), active osteoid deposition (**c1** and **c4** only, red staining) indicative of active bone formation and fibrous scar tissue often associated with medullary spaces (black stars). The dashed curve in **c1** shows the limit between the residual cell-free collagenic material (red star in **c1**) and mature bone formation including entrapped osteocytes. Residual material for the ceramics implant exists as ceramic particles (red star in **c2**) or voids reflecting the presence of ceramic particles probably released during the cutting step of thin-section preparation (red star in **c3**). Scale bars, 50 µm.

Preclinical bone grafts evaluation

Extending into clinical considerations, we synthesized Col-CHA using clinical-grade collagen (ColCG-CHA) (see Methods and characterization in Extended Data Fig. 7). The ColCG-CHA matrix was compared with two commercial crystalline mineral-based substitutes available as macroporous block (Vitoss, VO) and as macroporous granules (Mastergraft, MG) and to the AB gold standard (Extended Data Fig. 8) following the aforementioned ewe implantation procedure ($n = 12$ for ColCG-CHA and $n = 5$ for AB, VO and MG).

The rationale behind including two different types of ceramic (blocks and granules) was to discern the bone-formation response associated with the shape of the material. Ceramics being radiodense, a clear X-ray evaluation of the fraction area of mineralized bone formation remains challenging. The comparison between radiographic images and macroscopic observations of the defect (identified by white materials) clearly indicates that ceramic materials remained within the defect (Fig. 5a and Extended Data Fig. 8d). This observation may account for the thicker appearance of peripheral ossification observed with ceramics, in contrast to both ColCG-CHA and AB. Therefore, a histomorphological analysis focusing on bone mineralization, the presence of collagenic scar tissue and osteoblastic activity was deemed more suitable for this evaluation.

Quantitative and qualitative histological evaluation of non-decalcified sections (Supplementary Table 2 and Extended Data Fig. 9) reveal bone-healing processes in all of the samples, both at the periphery and within the centre of the defect (Fig. 5b,c). Specifically, the fraction area of mineralized bone formation within the defect measured on sections stained with von Kossa stain ranged from 23.7 ± 12.6 to 32.0 ± 17.4% for the ceramics (MG and VO, respectively), 32.8 ± 9.8 for AB and 30.4 ± 7.6% for ColCG-CHA. These values are close to that found for physiological trabecular bone, as measured in the adjacent

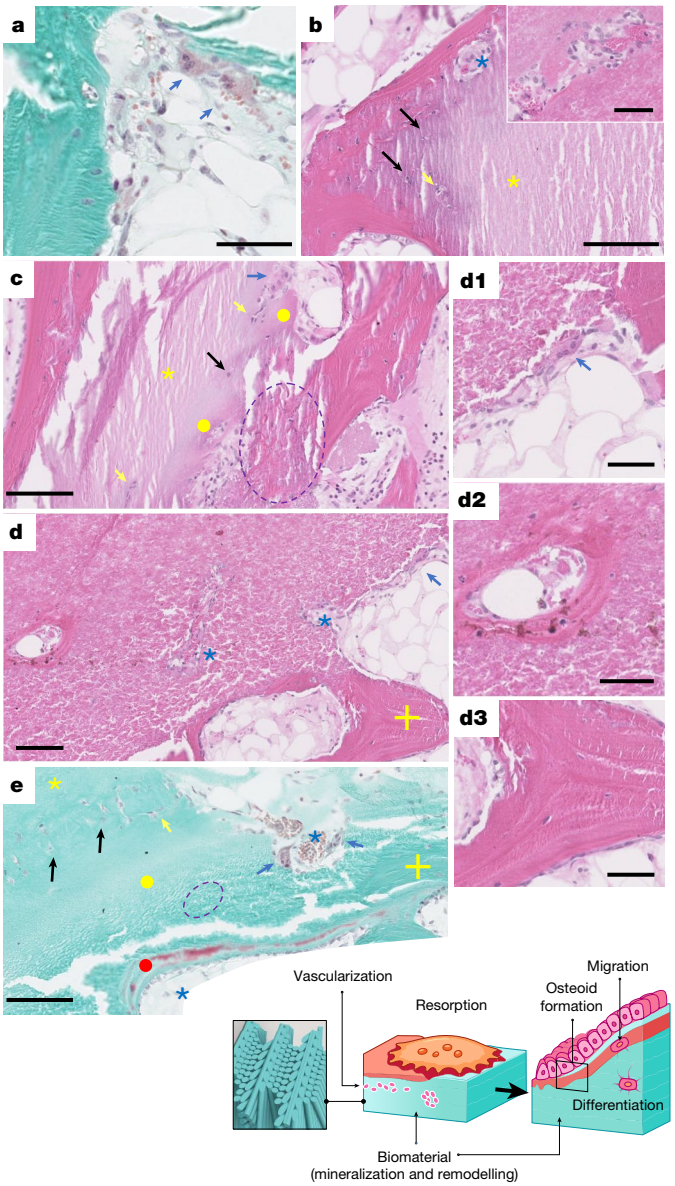

Fig. 6 | In-depth histopathological analysis of bone-like material implantation in ewe after 2 months. a, GT-stained histological thin section of implantation site with ColCG-CHA ($n = 12$ defects) showing the presence of active osteoclasts (blue arrows). Scale bar, 100 µm. **b**–**d**, HE histological thin sections of various areas in defects implanted with ColCG-CHA ($n = 12$ defects). The remnant material (yellow stars in **b** and **c**) is being infiltrated by vascular cells (isolated or grouped, black and yellows arrows, respectively, in **b** and **c**), whereas other regions take a granular aspect reminiscent of the in situ mineralization observed in the rat study (yellow dots in **c**). The higher-magnification inset in **b** shows a grouped vascular cells infiltration from another section. Blue star in **b** points to a more structured vascular formation. The dashed oval in **c** indicates an area of the mineralized remnant material reflecting a maturation towards a woven bone aspect that can then be further remodelled into mature bone. Such intermediate area is abundant in **d**. Remodelling is observed, including active osteoclasts (blue arrow and **d1**), small resorption lacunae and larger vascularized medullary spaces (blue stars and **d2**). The medullary spaces are surrounded by mature lamellar bone (yellow cross) with osteocytes and quiescent or active osteoblasts rows (**d3**). Scale bars, 100 µm (**b**,**c**,**d**), 50 µm (**b** inset,**d1**–**d3**) **e**, Histological GT-stained section and schematic representation of the main processes induced by bone-like biomaterials: (1) implant (yellow star) infiltration by vascular cells (black and yellow arrows) concomitantly with (2) in situ collagen mineralization (yellow dot); (3) evolution towards an intermediate bone-like aspect reminiscent of the structure of woven bone (dashed oval); (4) resorption by osteoclasts (blue arrows); (5) osteoblasts layer formation (mononuclear cuboid cells in pink) producing collagen fibrils (newly formed osteoid tissue in light blue and red), that is, active remodelling and bone formation (red dot) around large vascularized medullary spaces (blue stars); (6) mature bone formation (yellow cross) with osteoblasts migration/embedment, which may differentiate into osteocytes. Scale bar, 100 µm.

bone (Extended Data Fig. 10a–d). It is noteworthy that our focus was on assessing new bone formation, excluding mineral residues resulting from the non-degradation of ceramics. However, the use of von Kossa stain, which identifies divalent ions, prevents from distinctly differentiating between calcium from the matrix and that of the de novo mineralization[44].

In all four defects, mature and mineralized trabecular bone are observed, forming a regular network, as well as the presence of fibrous scarring tissue (Fig. 5c, black stars). However, the quantity of collagenic scar tissue is notably small (with a mean quantity of fibrous tissue scored as 1.2 for ColCG-CHA, 1.2 for AB, 0.8 for MG and 1.6 VO). This low score of fibrous reaction surrounding material suggests good biocompatibility of the implants, further supported by the remarkably low intensity of the peri-material inflammatory response (with a mean score 0.6 for ColCG-CHA, 0.4 for AB, 0.6 for MG and 1.4 VO).

An interesting discrepancy in bone-healing profiles is observed at the bone marrow–bone interface when comparing the composites (ColCG-CHA and AB; Fig. 5c1,c4) to the pure mineral-based materials (Fig. 5c2,c3). Both ColCG-CHA and AB exhibit regular osteoid layers (red staining) associated with active rows of osteoblasts (Fig. 5c1,c4, black arrows) along thick and multifocal connected bone trabeculae or along residual matrix plugs. By contrast, such osteoid layers are not observed within the implanted ceramics. Quantitatively, the extent of active bone formation (measured by the quantity of bone-forming cells—numerous clusters of osteoblasts—and osteoid deposition) is much higher for ColCG-CHA in comparison with the other biomaterials (osteoid activity scored 3.6 for ColCG-CHA versus 0.8–2 for ceramics and AB and measured by histomorphometry at 0.11% of the osteoid surface for ColCG-CHA-implanted defect versus 0.07% for AB and 0.09–0.11% for ceramics). The presence of nearby osteoclasts adjacent to the osteoid tissue strengthens the occurrence of an active bone-remodelling process in ColCG-CHA (Fig. 6a, blue arrows). Therefore, the simultaneous observation of osteoclastic resorption and multiple active osteoid layers ('coupled remodelling') in ColCG-CHA indicates the integration, colonization and continuing regeneration of the normal bone structure (for example, dashed curve in Fig. 5c1). This suggests that bone remodelling is more pronounced with delayed plasticity, potentially leading to more physiological reconstruction and better adaptation to mechanical stress, unlike the intense remodelling induced by growth factors[45]. Notably, the presence of active osteoid layers and the remodelling sequence bear resemblance to processes typically observed for AB. Further exploration could be highly valuable to understand the connection between the presence of such active osteoid layers and the osteoinductive properties of grafting materials.

Moreover, both ceramics show thin trabeculae with few connections within the trabecular network (Fig. 5c2,c3). The newly formed bone tissue in ceramics also exhibits much lower maturity compared with that observed in ColCG-CHA and AB (with an average maturity score ranging from 2.2 to 2.6 for ceramics versus 3.1 and 4.2 for ColCG-CHA and AB, respectively). These bone trabeculae are found at the interface with either a loosely non-mineralized fibrous tissue for MG or spherical voids in VO (black and red stars in Fig. 5c2,c3, respectively), indicating that ceramic particles were removed during the preparation of thin sections, that is, during the cutting step. Also, ceramic residues seen as grey/black granular deposits (Fig. 5c2, red stars and Extended Data Fig. 10e) are observed all over the samples, demonstrating incomplete degradation of the material according to the macroscopic observations

and to X-ray images. Notably, bone reconstruction seems frozen in ceramics, with 'passive' mature trabeculae (quiescent osteoblasts with little to no osteoid deposits; Fig. 5c3, black arrow) surrounding the ceramic residues, suggesting an inability to further adapt to local mechanical constraints. Nevertheless, the results confirm that ceramics are osteointegrated and osteoconductive[3,46].

These results have several implications. First, ceramic residues confirm that crystalline calcium phosphates are treated as a foreign material during bone reconstruction[47], highlighting the importance of using minerals with bone crystalline features and properties (for example, hydrophilicity)[36]. Second, open macroporosity in these materials is crucial for physiological fluid impregnation and host-cell colonization, ensuring osteoconductivity. However, bone and vascular cells possess all the biomolecules (for example, matrix metalloproteinases, non-collagenous proteins and collagen-binding integrins) to migrate through the tissue without requiring macropores[34]. This migration also occurs for ColCG-CHA, although this material is free of any host cells on implantation. Therefore, although macropores facilitate cell diffusion, they are not essential for collagen-based scaffold.

A comprehensive histopathological analysis of the ColCG-CHA integration mechanism was conducted using haematoxylin and eosin (HE) and Goldner trichrome (GT) staining (Fig. 6b–e). Observation of the remnant matrix (Fig. 6b,c,e, yellow star) reveals infiltration by numerous migrating cells, either isolated or in small groups, showing small branching lines (Fig. 6b,c,e, black and yellow arrows, respectively). Within these regions, ingrowth of capillaries filled with erythrocytes at various stages of development are observed (Fig. 6b,d,e, blue stars and inset), confirming that the dense collagen structure does not hinder cell migration, even without macropores, cells or growth factors supplementation. Notably, the absence of ischaemic lesions (for example, avascular necrosis/osteonecrosis) indicates proper vascularization. Direct evidence of successful vascularization includes the presence of morphologically mature and functional vascular structures, as evidenced by circulating erythrocytes in the lumen of the neovessels. This vascularization is required for biomaterials integration. Notably, some areas of the remnant material retain a more intense (basophilic) stain in HE staining and show a granular appearance without substantial structural changes (Fig. 6c,e, yellow dots). These areas are similar to the in situ mineralization observed in the rat study, as confirmed by von Kossa staining (Extended Data Fig. 10f). The area highlighted by the dashed oval in Fig. 6c reflects the conversion of such mineralized material into a bone-like matrix with a woven bone aspect (Fig. 6d), which is favourable for further remodelling and maturation.

In regions indicating later stages of bone maturity, the matrix shows increased degradation by resorption lacunae containing active osteoclasts (Fig. 6d,d1, blue arrows) and larger vascularized medullary spaces (Fig. 6d, blue stars and Fig. 6d2). Moreover, substantial portions of the implanted matrix have been replaced by lamellar mature bone (Fig. 6d, yellow cross and Fig. 6d3) encompassing osteocytes in their lacunae, covered by rows of quiescent or active osteoblasts and surrounded by bone marrow spaces. These mature-bone regions correspond to normal bone tissue and affix to the remnant matrix, indicating that the implant is undergoing remodelling towards mature bone. These observations are clearly highlighted by the various tinctorial affinities in HE staining, which discriminate areas with an 'initial aspect' (smooth appearance and homogeneous light pink) from those exhibiting mature bone (bright pink and mineralized). This integration mechanism closely resembles that observed in the rat study for the densest collagen matrix.

In line with general wound-healing principles, bone repair encompasses four main sequential steps: haematoma formation (haemostasis phase), followed by the fibrocartilaginous and subsequent bony callus formation (inflammation, angiogenesis and proliferative phases) and finally bony callus remodelling[48] (maturation phase). On the basis of histological observations, it is conceivable that our bone-like biomaterial may accelerate or bypass stages leading up to the remodelling. This hypothesis is supported by previous findings demonstrating that primary human osteoblasts seeded on similar materials exhibit migration and subsequent differentiation into osteocytes[34]. Building on these in vitro works and the present in vivo histological observations (Fig. 6e), we propose that our structurally designed bone-like biomaterial (yellow star) could enhance performance by: (1) supporting angiogenesis, cell attachment and migration (black and yellow arrows); (2) driving in situ mineralization[27] (yellow dot) and progressive conversion to a woven bone-like matrix (dashed oval); (3) enabling resorption by osteoclasts (blue arrows) and related enzymatic machinery supplied by angiogenesis (blue stars), allowing collagen digestion and remodelling; (4) facilitating the formation of active osteoid layers with osteoblasts (red dot) producing collagen fibrils; and (5) promoting osteoblasts migration, embedment and differentiation into osteocytes, leading to physiologically mature bone (yellow cross). The proposed mechanism for bone regeneration with our material is schematically outlined in Fig. 6e.

Taken together, these results provide the experimental evidence for the pivotal role of ECM microstructure in driving cellular behaviour[5] in bone.

Conclusion

This work differs from conventional regenerative medicine approaches that use cell-preloaded matrices[49], as our biomaterials are free of cells and any associated molecular machinery (such as non-collagenous proteins or growth factors). Using sophisticated bone biomaterials was crucial to demonstrate that the mineralized twisted plywood pattern stimulates bone formation and contributes to performance comparable with AB, with the structural aspect complementing the biological and mechanical ones[14]. This result reinforces the role played by physicochemical processes in bone physiology[50,51] and promising potential for application in bone replacement while also offering innovative models to investigate the interaction between materials and living tissues.

Online content

Any methods, additional references, Nature Portfolio reporting summaries, source data, extended data, supplementary information, acknowledgements, peer review information; details of author contributions and competing interests; and statements of data and code availability are available at https://doi.org/10.1038/s41586-024-08208-z.

1. Pape, H. C., Evans, A. & Kobbe, P. Autologous bone graft: properties and techniques. *J. Orthop. Trauma* **24**, S36–S40 (2010).
2. Giannoudis, P. V., Dinopoulos, H. & Tsiridis, E. Bone substitutes: an update. *Injury* **36**, S20–S27 (2005).
3. Bauer, T. W. & Muschler, G. F. Bone graft materials. An overview of the basic science. *Clin. Orthop. Relat. Res.* **371**, 10–27 (2000).
4. Discher, D. E., Mooney, D. J. & Zandstra, P. W. Growth factors, matrices, and forces combine and control stem cells. *Science* **324**, 1673–1677 (2009).
5. Engler, A. J., Sen, S., Sweeney, H. L. & Discher, D. E. Matrix elasticity directs stem cell lineage specification. *Cell* **126**, 677–689 (2006).
6. Discher, D. E., Janmey, P. & Wang, Y. Tissue cells feel and respond to the stiffness of their substrate. *Science* **310**, 1139–1143 (2005).
7. Matsugaki, A. et al. Abnormal arrangement of a collagen/apatite extracellular matrix orthogonal to osteoblast alignment is constructed by a nanoscale periodic surface structure. *Biomaterials* **37**, 134–143 (2015).
8. Park, Y. et al. Trabecular bone organoid model for studying the regulation of localized bone remodeling. *Sci. Adv.* **7**, eabd6495 (2021).
9. Chen, S. et al. Biomaterials with structural hierarchy and controlled 3D nanotopography guide endogenous bone regeneration. *Sci. Adv.* **7**, eabg3089 (2021).
10. Weiner, S. & Wagner, H. D. The material bone: structure-mechanical function relations. *Annu. Rev. Mater. Sci.* **28**, 271–298 (1998).
11. Seeman, E. & Delmas, P. D. Bone quality — the material and structural basis of bone strength and fragility. *N. Engl. J. Med.* **354**, 2250–2261 (2006).
12. Gupta, H. S. et al. Cooperative deformation of mineral and collagen in bone at the nanoscale. *Proc. Natl Acad. Sci.* **103**, 17741–17746 (2006).
13. Walsh, W. R. et al. Critical size bone defect healing using collagen–calcium phosphate bone graft materials. *PLoS One* **12**, e0168883 (2017).
14. Ghiasi, M. S., Chen, J., Vaziri, A., Rodriguez, E. K. & Nazarian, A. Bone fracture healing in mechanobiological modeling: a review of principles and methods. *Bone Rep.* **6**, 87–100 (2017).

15. Reznikov, N., Bilton, M., Lari, L., Stevens, M. M. & Kröger, R. Fractal-like hierarchical organization of bone begins at the nanoscale. *Science* **360**, eaa02189 (2018).
16. Giraud-Guille, M. M. Twisted plywood architecture of collagen fibrils in human compact bone osteons. *Calcif. Tissue Int.* **42**, 167–180 (1988).
17. Wang, Y. et al. Controlled collagen assembly to build dense tissue-like materials for tissue engineering. *Soft Matter* **7**, 9659–9664 (2011).
18. Lama, M. et al. Self-assembled collagen microparticles by aerosol as a versatile platform for injectable anisotropic materials. *Small* **16**, 1902224 (2020).
19. Giraud-Guille, M. M. Liquid crystallinity in condensed type I collagen solutions: a clue to the packing of collagen in extracellular matrices. *J. Mol. Biol.* **224**, 861–873 (1992).
20. Wang, Y. et al. The predominant role of collagen in the nucleation, growth, structure and orientation of bone apatite. *Nat. Mater.* **11**, 724–733 (2012).
21. Nunamaker, D. M. Experimental models of fracture repair. *Clin. Orthop. Relat. Res.* **355**, S56–S65 (1998).
22. Moreno-Jiménez, I. et al. Human and mouse bones physiologically integrate in a humanized mouse model while maintaining species-specific ultrastructure. *Sci. Adv.* **6**, eabb9265 (2020).
23. Kerschnitzki, M. et al. The organization of the osteocyte network mirrors the extracellular matrix orientation in bone. *J. Struct. Biol.* **173**, 303–311 (2011).
24. Colombier, M. L. et al. A single low dose of RGTA, a new healing agent, hastens wound maturation and enhances bone deposition in rat craniotomy defects. *Cells Tissues Organs* **164**, 131–140 (1999).
25. Blanquaert, F. et al. Heparan-like molecules induce the repair of skull defects. *Bone* **17**, 499–506 (1995).
26. Bohner, M. & Miron, R. J. A proposed mechanism for material-induced heterotopic ossification. *Mater. Today* **22**, 132–141 (2019).
27. van der Meijden, R. H. et al. A 3D cell-free bone model shows collagen mineralization is driven and controlled by the matrix. *Adv. Funct. Mater.* **33**, 2212339 (2023).
28. Manolagas, S. C. & Jilka, R. L. Bone marrow, cytokines, and bone remodeling — emerging insights into the pathophysiology of osteoporosis. *N. Engl. J. Med.* **332**, 305–311 (1995).
29. Nassif, N. et al. Self-assembled collagen–apatite matrix with bone-like hierarchy. *Chem. Mater.* **22**, 3307–3309 (2010).
30. Ramtani, S., Takahashi-Iniguez, Y., Helary, C., Geiger, D. & Guille, M. M. G. Mechanical behavior under unconfined compression loadings of dense fibrillar collagen matrices mimetic of living tissues. *J. Mech. Med. Biol.* **10**, 35–55 (2010).
31. Marelli, B., Ghezzi, C. E., Barralet, J. E. & Nazhat, S. N. Collagen gel fibrillar density dictates the extent of mineralization in vitro. *Soft Matter* **7**, 9898–9907 (2011).
32. Brighton, C. T. & Hunt, R. M. Histochemical localization of calcium in the fracture callus with potassium pyroantimonate. Possible role of chondrocyte mitochondrial calcium in callus calcification. *J. Bone Joint Surg.* **68**, 703–715 (1986).
33. Tsigkou, O. et al. Engineered vascularised bone grafts. *Proc. Natl Acad. Sci.* **107**, 3311–3316 (2010).
34. Robin, M. et al. Involvement of 3D osteoblast migration and bone apatite during in vitro early osteocytogenesis. *Bone* **88**, 146–156 (2016).
35. Paris, M. et al. Scaffold curvature-mediated novel biomineralization process originates a continuous soft tissue-to-bone interface. *Acta Biomater.* **60**, 64–80 (2017).
36. Wang, Y. et al. Water-mediated structuring of bone apatite. *Nat. Mater.* **12**, 1144–1153 (2013).
37. Nassif, N. et al. In vivo inspired conditions to synthesize biomimetic hydroxyapatite. *Chem. Mater.* **22**, 3653–3663 (2010).
38. Von Euw, S. et al. Bone mineral: new insights into its chemical composition. *Sci. Rep.* **9**, 8456 (2019).
39. Nuss, K. M. R., Auer, J. A., Boos, A. & von Rechenberg, B. An animal model in sheep for biocompatibility testing of biomaterials in cancellous bones. *BMC Musculoskelet. Disord.* **7**, 67 (2006).
40. Sparks, D. S. et al. A preclinical large-animal model for the assessment of critical-size load-bearing bone defect reconstruction. *Nat. Protoc.* **15**, 877–924 (2020).
41. Glimcher, M. J. Bone: nature of the calcium phosphate crystals and cellular, structural, and physical chemical mechanisms in their formation. *Rev. Mineral. Geochem.* **64**, 223–282 (2006).
42. Liu, S. et al. Bioinspired collagen-apatite nanocomposites for bone regeneration. *J. Endod.* **42**, 1226–1232 (2016).
43. Liu, Y. et al. Hierarchically staggered nanostructure of mineralized collagen as a bone-grafting scaffold. *Adv. Mater.* **28**, 8740–8748 (2016).
44. Boskey, A. L. Matrix proteins and mineralization: an overview. *Connect. Tissue Res.* **35**, 357–363 (1996).
45. Liu, T., Wu, G., Wismeijer, D., Gu, Z. & Liu, Y. Deproteinized bovine bone functionalized with the slow delivery of BMP-2 for the repair of critical-sized bone defects in sheep. *Bone* **56**, 110–118 (2013).
46. Albrektsson, T. & Johansson, C. Osteoinduction, osteoconduction and osseointegration. *Eur. Spine J.* **10**, S96–S101 (2001).
47. Li, X., Zou, Q., Chen, H. & Li, W. In vivo changes of nanoapatite crystals during bone reconstruction and the differences with native bone apatite. *Sci. Adv.* **5**, eaay6484 (2019).
48. Sheen, J. R. & Garla, V. V. *Fracture Healing Overview* (StatPearls, 2022).
49. Park, H. et al. Acellular dense collagen-S53P4 bioactive glass hybrid gel scaffolds form more bone than stem cell delivered constructs. *Mater. Sci. Eng. C* **120**, 111743 (2021).
50. Robin, M. et al. Acidic osteoid templates the plywood structure of bone tissue. *Adv. Sci.* **11**, 2304454 (2024).
51. Chaudhuri, O., Cooper-White, J., Janmey, P. A., Mooney, D. J. & Shenoy, V. B. Effects of extracellular matrix viscoelasticity on cellular behaviour. *Nature* **584**, 535–546 (2020).

Methods

Matrix preparation

Collagen extraction. Type I collagen monomers were extracted from rat tail tendons following a classical procedure. Fresh tendons were washed with phosphate-buffered saline solution and solubilized in 0.5 M acetic acid. The raw solution was centrifuged and the supernatant was selectively precipitated with 0.7 M NaCl. Precipitated type I collagen was solubilized in 0.5 M acetic acid and then desalted by dialysis against 0.5 M acetic acid. The concentrations of type I collagen solutions were assessed by hydroxyproline titration and adjusted to a final stock concentration of approximately 3 mg ml^{-1}.

Matrix synthesis. All of the experiments were carried out at room temperature (19 ± 2 °C) to prevent collagen denaturation and sterility was kept throughout the procedure. The matrices were stored in distilled water at 4 °C before implantation.

Col40 (rat model). The collagen solution was progressively concentrated up to 40 mg ml^{-1} by slow evaporation of the solvent in a safety cabinet[52]. Then, fibrillogenesis in vitro was performed under ammonia vapours for 24 h. This step allows the stabilization of the liquid-crystalline organization into dense fibrillar matrices[53]. Finally, matrices were punched with an 8-mm steel trepan and rinsed with sterile phosphate-buffered saline until neutralization of the pH.

Col100 (rat model). Below the critical concentration of 40 mg ml^{-1}, type I collagen molecules do not organize[52]. However, above this threshold concentration, they undergo a spontaneous transition into ordered liquid-crystalline phases owing to the lyotropic properties of acidic type I collagen solution in vitro[19]. After a sol–gel transition leading to collagen fibril formation, the geometries of fibrillary networks closely mimic those found in living tissues, depending on the targeted concentration (at least 80 mg ml^{-1} for cholesteric bone-like mesophase)[53,54]. The Col100 matrix was prepared using a procedure that combines injection and reverse-dialysis processes to increase the collagen concentration[17]. A 15 ml volume of about 1 mg ml^{-1} soluble acidic collagen solution (0.5 mM acetic acid) was continually injected (rate range 1 µl min^{-1} to 15 ml min^{-1}) in a closed dialysis chamber (3 mm thickness and 10 mm width) for 8 days. The bottom of the chamber contained a dialysis membrane with a molecular weight cut-off of 12–14 kDa. The reverse-dialysis process was set against polyethylene glycol (35 kDa, Fluka) dissolved in 0.5 M acetic acid up to about 150 mg ml^{-1}. The flow of the collagen solution was controlled to maintain the same pressure on each side of the dialysis membrane. After injection, dialysis was continued for 8 days, to obtain a homogeneous concentration in the samples. The pH was then increased to a range of 9–10 by ammonia gas diffusion for 4 days to induce collagen fibrillogenesis and stabilize the liquid-crystalline organization into dense fibrillar matrices[29]. The matrices were then removed from the dialysis chamber and washed several times in double-distilled water until neutralization. Finally, matrices were punched with an 8-mm steel trepan before implantation.

Col (ewe model). The procedure matched the Col100 matrix except that: (1) the initial volume of the acid solution was 30 ml and (2) the mould dimensions were diameter 8 mm and depth 13 mm. Here the process to elaborate the materials ends with the removal of the stabilized fibrillar matrix directly from the mould that allows the shaping of the collagen construct.

Col-CHA (ewe model). The Col-CHA matrix was prepared as follows: a volume of a 3 mg ml^{-1} soluble acidic collagen solution (0.5 mM acetic acid) was mixed with a $CaCl_2/NaH_2PO_4/NaHCO_3$ acidic solution (0.5 mM acetic acid). According to a previously described procedure (col/CHA in ref. 20), the procedure is consistent with the synthesis of preferentially B-type CHA, which has a formula of $Ca_{10-x}(PO_4)_6{-}x(CO_3)x(OH)_2{-}x$ with $0 \le x \le 2$. The pH was adjusted to 2.2. The final concentration of the collagen solution was about 1 mg ml^{-1} and the final ionic strength was 165.9 mM. The procedure matched the Col matrix except that the initial volume of the acid solution was 30 ml.

ColCG-CHA (ewe model). The procedure matched the Col-CHA matrix except that commercial acidic clinical-grade collagen was used instead of collagen extracted from rat tail tendons to avoid inflammatory response. Bovine skin type I collagen diluted in acetic acid at a concentration of 5 mg ml^{-1} was purchased from Symatese (reference ACI070). The use of clinical-grade collagen was chosen to eliminate any potential immunologic responses arising from variations in collagen-purification processes[55], thereby enabling the evaluation of our samples as potential bone biomaterials. Although both collagen solutions exhibit lyotropic properties and the ability to form fibrils necessary to produce high-density twisted plywood collagen matrices, clinical-grade collagen demonstrates higher purity and greater thermal stability (see Extended Data Fig. 7).

Commercially available mineral-based substitutes. Vitoss 1.2 cc blocks (reference 2102-0013 Stryker) is composed of a porous (up to 90%) structure of β-tricalcium phosphate. The Vitoss block was shaped with a scalpel to fit the defect. Mastergraft 5cc Granules (reference 7600105, Medtronic) is composed of 80% porous resorbable ceramic granules (15% HA, 85% β-tricalcium phosphate).

Autologous bone. AB fragments were extracted from iliac crest. The animal's own blood serum was kept and the fragments were subsequently used as bone filler.

Reference human bone sample for SEM and TEM. The bone samples observed by SEM in Fig. 1a,b and by TEM in Fig. 3c were prepared as part of a previous study[56].

Bone powder. The organic matrix (collagen and other proteins) was removed from bone sample by immersion in dilute NaClO aqueous solution treatment to extract the mineral particles (Extended Data Fig. 1), as previously described[36].

Matrix characterization

SEM and elemental characterizations. Collagen matrices were fixed in 2.5% glutaraldehyde in a cacodylate solution (0.05 M). After washing in a cacodylate/saccharose buffer solution (0.05 M/0.6 M, pH 7.4), dehydration in increasing ethanol baths, matrices were dried at the carbon dioxide critical point using a Leica EM CPD300. Samples coated with a 10 nm gold layer were observed in a Hitachi S-3400N at an accelerating voltage of 10 kV.

TEM. Matrices were fixed in glutaraldehyde, washed and dehydrated as described for SEM and embedded in araldite. The matrices prepared without mineral (Col40, Col100 and Col) were also post-fixed with 2% osmium tetroxide for 1 h at 4 °C before dehydration. Ultrathin sections (70 nm) were obtained, stained with uranyl acetate and observed in a FEI Tecnai G2 Spirit TWIN electron microscope operating at 120 kV.

WAXD (transmission mode). Small parts of the mineral matrices were cut out of the bulk sample and inserted in X-ray cylindrical borosilicate capillary tubes. The tubes were flame-sealed to keep the samples hydrated and then placed directly in the vacuum chamber beam. X-ray diffraction experiments were performed with a S-MAX 3000 RIGAKU using a monochromatic CuKα radiation. The data were collected in the 5–60° range (2θ). The sample-to-detection distance was 0.059 m. The data were analysed using FIT2D (version 18, beta) software. The 2D WAXD patterns were collected with imaging plates and then

scanned with 50 µm resolution. The diameter of the cylindrical beam dimension at the specimen was 400 µm and the sample thickness was approximately 1 mm.

Differential scanning calorimetry. Experiments were performed on a TA Q20 apparatus. The heating rate was set at 5 °C min^{-1} and the temperature ranged from 25 °C to 55 °C. About 20 mg of sample was weighed and put in an aluminium pan, the reference being an empty sealed aluminium pan. Collagen purity is determined on the basis of thermal stability. Collagen solutions typically exhibit an endothermic peak around 40 °C, indicating denaturation into gelatine that occurs through the irreversible unfolding of the triple helix[57].

Polarized light microscopy. The materials were placed, without any treatment, between a glass slide and a coverslip. Observations were made using a transmission Zeiss Axio Imager A2 POL. The microscope was equipped with the standard accessories for examination of birefringent samples under polarized light (that is, crossed polars) and an Axiocam CCD camera.

SDS-PAGE. Sodium dodecyl sulfate–polyacrylamide gel electrophoresis (SDS-PAGE) of type I collagen extracted from rat tail tendons and bovine dermis (clinical grade) was performed, using an acrylamide (10%)/bis-acrylamide (30%) gel in the presence of tris-HCl 1.5 M (pH 8.8), SDS, EDTA, glycerol and 2-mercaptoethanol. Migration was checked by adding bromophenol blue to the samples (0.05%). The separated protein bands were identified by comparison with a standard molecular mixture marker (Sigma-Aldrich) including the α chain of type I collagen (125.103 KDa).

Mechanical characterization. The local Young's modulus E of the Col40, Col100 and Col-CHA matrices was estimated at room temperature (22 °C) through microindentation (Piuma Nanoindenter, Optics 11 Life). To this aim, the Col40 and Col100 matrices were used as is (see Fig. 2c), whereas the Col-CHA matrix shown in Fig. 3e was cut into a piece of thickness about 1 mm. These matrices were immersed in their conservation medium at the bottom of a small Petri dish and their upper surface was indented using a spherical glass probe of radius R attached to a cantilever of calibrated stiffness k, with $R = 105$ µm and $k = 0.45$ N m^{-1} for Col40 and $R = 51$ µm and $k = 0.26$ N m^{-1} for Col100 and Col-CHA. Depending on the sample, these indentation tests involved forces ranging from 0.15 µN to 1.2 µN and penetration depths of 0.5–12 µm at the end of the loading phase, and to contact radii of 5–30 µm between the probe and the matrix. For each sample, about 200 independent indentations spaced by 50–200 µm were performed and each force–depth curve was fitted by a Hertzian contact model, yielding the effective Young's modulus E_{eff} at the locus of the indent. The local Young's modulus E was then computed through $E = E_{eff}(1 - \nu^2)$, assuming a Poisson ratio ν of 0.5 for all samples. The statistical analysis of the Young's modulus data was performed using MATLAB (release R2018b) software.

Implantations

Rat calvaria critical-size defect. The study was reviewed and approved by the Animal Care Committee of the University Paris Descartes (no. P2.JLS.174.10) The 30 8-week-old (220–240 g) male Wistar rats used in the study were housed in individual cages at stable conditions in the animal facility of the Laboratoire Pathologies, Imagerie et Biothérapies Orofaciales, Université Paris Cité. The surgical procedures were performed as described previously[24,25,58]. After anaesthesia with an intraperitoneal injection of 100 mg per kg body weight of ketamine and 10 mg per kg body weight of xylazine hydrochloride (Centravet Alfort), the cranial area was shaved, disinfected and the skin was incised in the sagittal direction. The periosteum was then incised in the same direction and elevated to expose the underlying calvaria. An 8-mm defect was created in the centre of the calvaria using a steel trephine mounted on a low-speed dental handpiece, under sterile saline irrigation. The defects were randomly filled with dense collagen matrices, either twisted plywood organized fibrils (100 mg ml^{-1}; Col100, $n = 10$) or randomly dispersed fibrils (40 mg ml^{-1}; Col40, $n = 10$) or left empty (controls $n = 8$). The skin flap was then replaced and secured with interrupted sutures. After 10 weeks, rats were anaesthetized as previously and euthanized using exsanguination. The skulls were removed and fixed in 70% ethanol. Three animals were excluded from further analysis: in the control group, one animal died and another had an incomplete defect created during the surgical procedure; in the Col100 group, one animal had its underlying dura mater and mid-sagittal sinus damaged, thus introducing a technical bias.

Radiomorphometric analysis (rat). The skulls were radiographed (exposure 13 kV, 12 mA, 15 min) in a microradiography unit (model Sigma 2060, CGR) with X-ray film (Kodak Professional Films). Morphometry was performed at a constant magnification with a semi-automatic image analyser coupling the microscope to a video camera and a computer. The percentage of bone-defect closure, corresponding to the percentage of radiopacity in skull defect, was calculated as the following ratio: area of radiopaque formation in the defect/area of the defect created by trephination × 100 using ImageJ software (v1.52a).

µCT. µCT was performed in IMOSAR, Laboratoire de Biologie, Bioingénierie et Bioimagerie Ostéo-articulaires (B3OA), UMR CNRS 7052 INSERM U1271, Université de Paris. Representative samples were scanned using a desktop micro-X-ray computed tomography (Micro-CT SkyScan 1172, Bruker), source voltage 59 kV, source current 100 µA, image pixel size 17.77 µm. Each sample was rotated 180° with a rotation step of 0.7°, exposure time 90 ms. 3D reconstruction and analysis were made with NRecon SkyScan software 1.7.1.6 (Bruker).

Statistical analysis. Given the high variability of the in vivo response and the related small sample size, the Kruskal–Wallis test ($\alpha = 0.05$, no correction, multiple comparison using the Mann–Whitney test) was used to assess overall differences between groups owing to its robustness in handling nonparametric data, whereas independent two-sided pairwise comparisons using the Mann–Whitney U test were performed to detect any potential trends or variations between specific groups. The results were discussed following two levels of significance. Differences were considered strictly significant if $P < 0.05$, whereas a $P < 0.10$ indicates a trend in the data. The statistical tests conducted in this study are indicated in the figure legends as follows: $^{*}P < 0.05$ and $^{**}P < 0.10$. Data are given as mean ± s.d.

Histomorphometric analysis (rat). After dehydration, the explants were embedded without demineralization in methyl methacrylate (Merck). 4-µm-thick sections were cut in the frontal plane with a Polycut E microtome (LEICA) in the central part of the defect. Sections were stained with toluidine blue, von Kossa or processed for enzyme histochemistry (Extended Data). Morphometry was performed at a constant magnification with a semi-automatic image analyser coupling the microscope to a video camera and a computer. TRAP sections were used to count the number of osteoclasts by millimetre based on 1/10th of the section. The von Kossa staining was used to quantify the percentage of mineralized tissue in the defect, calculated as the following ratio: area of matrix-related mineralized tissue/area of the defect × 100.

Enzyme histochemistry (rat). ALP activity was revealed with naphthol AS-TR phosphate (Sigma-Aldrich) and diazoted Fast Blue RR (Sigma-Aldrich). TRAP was detected using Fast Red TR Salt (Sigma-Aldrich) and naphthol AS-TR phosphate (Sigma-Aldrich).

SEM characterization of histological sections. Unstained bone histological thin sections were coated with 10 nm of carbon and imaged with

a Hitachi S-3400N scanning electron microscope with an accelerating voltage of 10 kV. Energy-dispersive X-ray spectroscopy was performed using an Oxford Instruments X-Max detector (20 mm^2). Using SEM to characterize histological sections is useful to visualize the in situ mineralization in which the fibrillar collagen matrix disappears in favour of mineral aggregates[59,60].

Ewe critical-size defect surgical procedure. Two studies were conducted on ewe. Both studies were reviewed and approved by the IMM Recherche's Institutional Animal Care and Use Committee before the initiation of this study. The Animal Care and Use Committee of the IMM Recherche is registered at the CNREEA under the Ethics Committee no. 37. The animal research centre (IMM Recherche) received an agreement (no. 75-14-01) by the Direction Départementale de la Protection des Populations. The studies were also performed in compliance with the Principles of Laboratory Animal Care, formulated by the National Society for Medical Research, and the Guide for the Care and Use of Laboratory Animals, by the Institute for Laboratory Animal Resources (published by the National Academies Press), as amended by the Animal Welfare Act of 1970 (P.L. 91-579) and the 1976 amendments to the Animal Welfare were followed. The surgical procedures were performed as described in ref. 39. This model for bone-defect reconstruction differs from the healing process of larger load-bearing defects, which often necessitate a further specific procedure, such as fixation plate[61]. A total of eight hole defects (diameter 8 mm, depth 13 mm) per animal (two animals for a total of 16 for ewe study no. 1 and six animals for a total of 48 for ewe study no. 2) were created with a drill into the distal and proximal metaphysis of the humerus and femur. After washing the bone cavity with saline solution, the holes were randomly left empty to heal or fill with the different materials (ewe study no. 1: Col and Col-CHA, $n = 5$ each; ewe study no. 2: ColCG-CHA $n = 12$, VO, MG and AB, $n = 5$ each). Then, the wound was covered with the adjacent tissues and the skin was stapled. Two months after surgery, the sheep were euthanized and both femoral and humeral bones were collected, freed from all overlying tissues and the drill holes were identified. Bone samples were cut perpendicular to the original drill hole.

Faxitron X-ray radiographic imaging. Bone samples were imaged with a cabinet X-ray system to screen, track and evaluate structural, bone density and bone distribution changes using a Faxitron system. Transversal slices of bones taken from the implant sites were submitted to X-ray analysis using Faxitron SR v1.5.

Scanner imaging. Bone samples were submitted to computed tomography scan analysis to investigate 3D reconstruction of the implants sites using a 256 Slice GE Revolution CT Scanner and observed with RadiAnt DICOM Viewer 2022.1.1.

Radiological image analysis. ImageJ software (v1.52a) was used to blindly analyse radiographic images from the rat experiment and Faxitron X-ray and scanner images from the first ewe experiment. First, each image was converted to greyscale and a grey-level threshold was set to discriminate radiopaque and non-radiopaque areas. Then, an area corresponding to the original defect size was set. Pixels with grey level above the threshold, corresponding to radiopaque bone, were counted and divided by the total amount of pixels in the selected area to obtain a bone-filling percentage. For scanner, as full depth acquisition was performed, several relevant images were analysed and the result was expressed as a mean to represent the bone filling of the entire depth of the defect.

Bone histological preparation (ewe). Samples were fixed in 4% paraformaldehyde solution, dehydrated with increasing ethanol baths and immersed for a week in a solution of butyl methacrylate, methyl benzoate, polyethylene glycol and benzoyl peroxide resin. Polymerization was triggered by the addition of N,N-dimethyl-toluidine and the samples were placed at −20 °C for 48 h. Serial thin sections (4–8 µm) were cut using tungsten carbide knives. Thereafter, the resin was removed using 2-ethoxyethyl acetate and the sections were rehydrated. The sections were then stained for the identification of tissue components in light microscopy analysis, scanned and observed using NDP.view2.8.24.

Histochemical staining. GT (haematoxylin, fuchsine, light green). The sections were immersed in haematoxylin Weigert solution. After washing, the sections were stained with Ponceau fuchsine. Non-specific staining areas were washed with a 1% phosphomolybdic acid solution. Subsequently, the sections were stained with a light-green solution. After a washing step, the sections were dehydrated with ethanol (increasing gradient) and xylene solutions and then mounted with a resin mounting liquid. Using GT, mineralized bone is stained in green, osteoid in red/orange, nuclei in blue and cytoplasm in light red.

von Kossa/Van Gieson staining. Sections were preincubated with 1% silver nitrate solution under ultraviolet light. Then, the non-specific staining patches were washed with 5% sodium thiosulfate solution. The sections were counterstained with Van Gieson picrofuscine. After a washing step, the sections were dehydrated with ethanol (increasing gradient) and xylene solutions and then mounted with resin mounting fluid. After von Kossa staining, calcium deposits are highlighted in brown-black, osteoid in red and other tissue in yellow.

Haematoxylin–eosin. Sections were immersed in haematoxylin solution. Then, they were rinsed and stained with a 1% eosin solution. After a washing step, the sections were dehydrated with ethanol (increasing gradient) and xylene solutions and then mounted with resin mounting fluid. After HE staining, nuclei are stained purple, cytoplasm pink and collagen pink-red.

Histomorphometry. On the basis of GT and von Kossa-stained histological sections, image analysis (ImageJ2 software v2.0.0) allowed measurement of (1) the amount of mineralized newly formed bone into the defect (mineralized bone surface/total surface) after exclusion of residual biomaterials and (2) the amount of osteoid tissue into the defect (osteoid surface/total surface).

Reporting summary

Further information on research design is available in the Nature Portfolio Reporting Summary linked to this article.

Data availability

Radiographies, scanner files, micro-computed tomography scans and histological raw imaging of all the samples included in this work are available on request to the corresponding author. All other data are available in the main text or in the Extended Data.

52. Giraud-Guille, M. M. & Besseau, L. Banded patterns in liquid crystalline phases of type I collagen: relationship with crimp morphology in connective tissue architecture. *Connect. Tissue Res.* **37**, 183–193 (1998).
53. Besseau, L. & Giraud-Guille, M. M. Stabilization of fluid cholesteric phases of collagen to ordered gelated matrices. *J. Mol. Biol.* **251**, 197–202 (1995).
54. Giraud-Guille, M. M, Nassif, N. & Fernandes, F. M. in *Materials Design Inspired by Nature: Function Through Inner Architecture* (eds Fratzl, P., Dunlop, J. W. C. & Weinkamer, R.) 107–127 (RSC Publishing, 2013).
55. Salameh, C. et al. Origin of transparency in scattering biomimetic collagen materials. *Proc. Natl Acad. Sci.* **117**, 11947–11953 (2020).
56. Giraud-Guille, M. M. Cholesteric twist of collagen *in vivo* and *in vitro*. *Mol. Cryst. Liq. Cryst.* **153**, 15–30 (1987).
57. Miles, C. A., Burjanadze, T. V. & Bailey, A. J. The kinetics of the thermal denaturation of collagen in unrestrained rat tail tendon determined by differential scanning calorimetry. *J. Mol. Biol.* **245**, 437–446 (1995).
58. Vigier, S. et al. Dense fibrillar collagen matrices sustain osteoblast phenotype in vitro and promote bone formation in rat calvaria defect. *Tissue Eng. Part A* **17**, 889–898 (2011).
59. Mckee, M., Buss, D. J. & Reznikov, N. Mineral tessellation in bone and the stenciling principle for extracellular matrix mineralization. *J. Struct. Biol.* **214**, 107823 (2022).
60. Shah, F. A., Ruscsák, K. & Palmquist, A. Transformation of bone mineral morphology: from discrete marquise-shaped motifs to a continuous interwoven mesh. *Bone Rep.* **13**, 100283 (2020).
61. Reichert, J. C. et al. A tissue engineering solution for segmental defect regeneration in load-bearing long bones. *Sci. Transl. Med.* **4**, 141ra93 (2012).

Acknowledgements We thank the IMOSAR, Laboratoire de Biologie, Bioingénierie et Bioimagerie Ostéo-articulaires (B3OA), UMR CNRS 7052 INSERM U1271, Université de Paris for the micro-computed tomography imaging, C. Torrens and M. Selmane for technical help, L. Cailleau for the plywood illustration, A. P. Hammersley and the ESRF for the use of FIT2D and S. Von Euw and P. Zaslansky for comments after reading the manuscript. We also acknowledge the DRITT (UPMC), particularly E. Bastin, and I. Coquilleau, as well as SATT Lutech, for financial support. N.N. thanks the Fondation du Collège de France and Fondation EDF for their support, especially M. Cheron for her valuable insights and trust.

Author contributions Conceptualization: M.-M.G.-G., A.M.-P., M.-L.C., N.N. Methodology: M.R., J.-L.S., G.P.-D., L.B., L.C., A.M.-P., F.B., M.-L.C., N.N. Investigation: M.R., E.M., G.C.D., Y.W., G.P.-D., T.D., S.M., L.B., L.C., F.B., M.-L.C., N.N. Visualization: M.R., G.C.D., J.-L.S., G.P.-D., L.C., F.B., M.-L.C., N.N. Funding acquisition: D.C., M.-M.G.-G., A.M.-P., N.N. Supervision: N.N. Writing – original draft: M.R., F.B., M.-L.C., N.N. Writing – review and editing: M.R., E.M., T.D., S.M., L.B., M.-M.G.-G., F.B., M.-L.C., N.N.

Competing interests The authors declare no competing interests.

Additional information

Supplementary information The online version contains supplementary material available at https://doi.org/10.1038/s41586-024-08208-z.

Correspondence and requests for materials should be addressed to Nadine Nassif.

Peer review information *Nature* thanks the anonymous reviewers for their contribution to the peer review of this work.

Extended Data Fig. 1 | Picture of bone powder. Mineral extracted from porcine bone with NaClO aqueous solution.

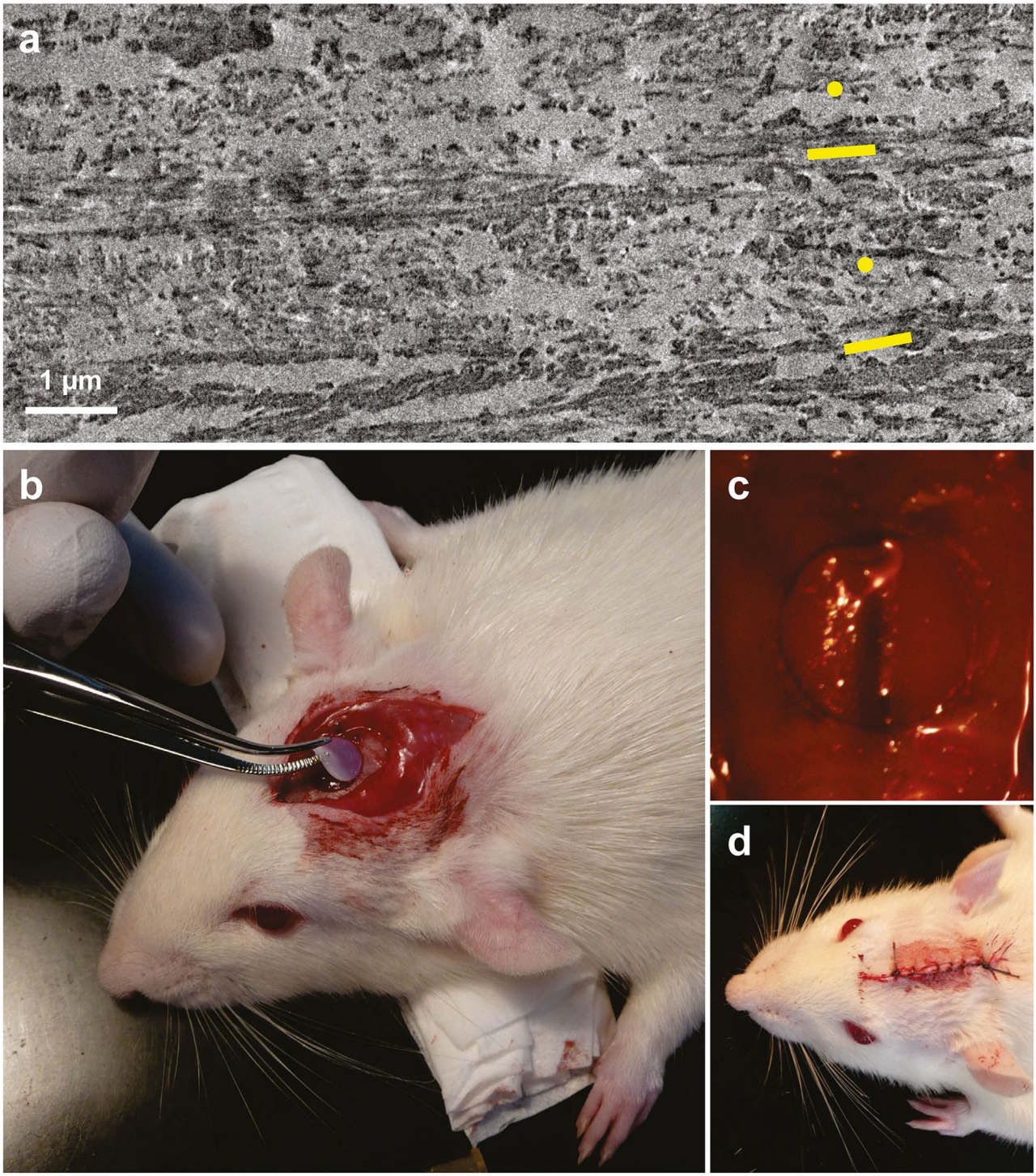

Extended Data Fig. 2 | Microstructure of collagen fibrils in bone extracted from rat calvaria and related rat calvaria critical-size defect surgical procedure. a, TEM image of bone ultrathin section extracted from the rat calvaria (Fig. 2c, $n = 1$ sample) showing dense fibrillar layers of different orientations. Yellow dots and bars represent fibrils that are perpendicular and parallel to the observation plan, respectively. Picture of circular-shaped collagen matrix fitting the calvaria defect in rat (**b**), the matrix adhering to the surrounding bone after several minutes (**c**) and the skin sutured (**d**).

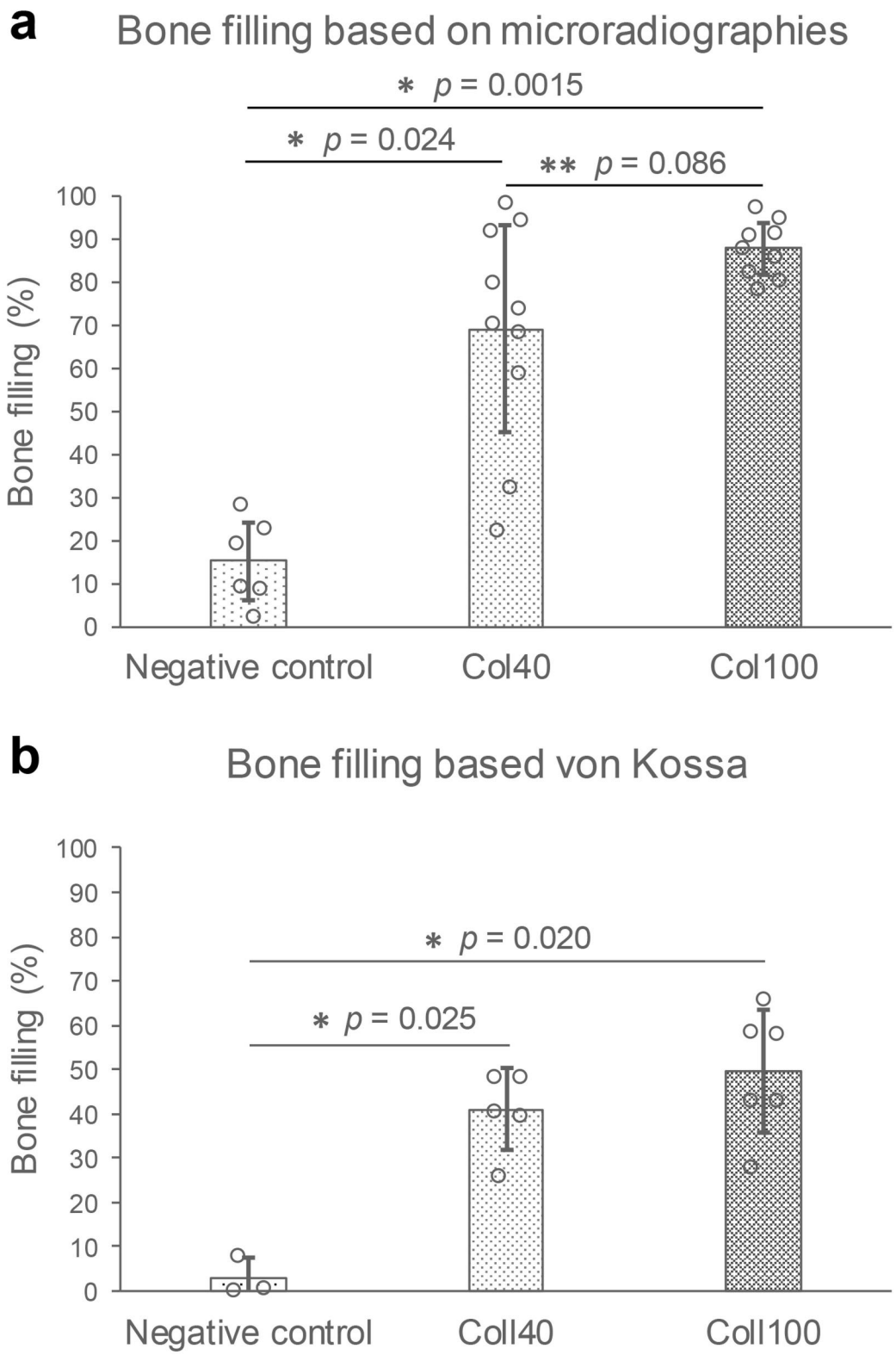

Extended Data Fig. 3 | Bone filling for rat experiment. Bone filling on the basis of microradiographies (**a**) and von Kossa-stained thin sections (**b**). The percentage of bone filling for each defect was blindly measured on individual images. Microradiograph data were analysed from the total number of animals included in each group, as indicated in the bars (n = 6, 10 and 9 for negative control, Col40 and Col100, respectively). von Kossa data were analysed from representative animals in each group, as indicated in the bars (n = 3, 5 and 6 for negative control, Col40 and Col100, respectively). Data were expressed as mean ± s.d. and compared using nonparametric Kruskal–Wallis with two-sided Mann–Whitney multiple comparison test. *Significant difference with $P < 0.05$. **A difference/trend with $P < 0.10$.

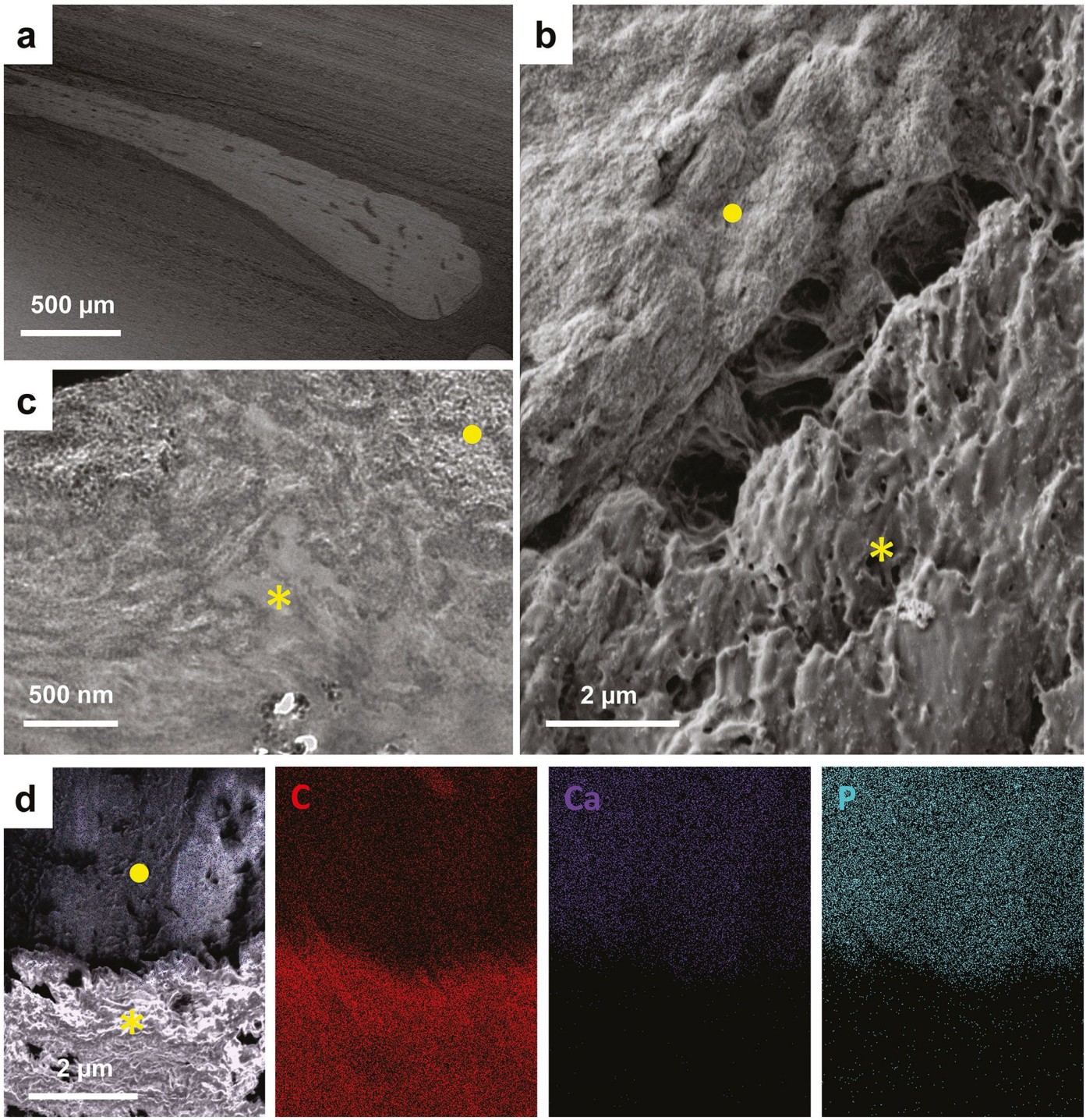

Extended Data Fig. 4 | Characterization of the in situ mineralization in the collagen materials implanted in rat calvaria model. SEM observations of a histological section from a defect implanted with Col100 ($n = 1$ sample) at low (**a**) and higher (**b**) magnifications. The interface in which in situ mineralization occurs (yellow dot, granular aspect) is clearly observed, the fibrillar aspect of the matrix (yellow star) disappearing in favour of mineral aggregates (refs. 59,60). **c**, This difference of texture is also seen at the TEM scale ($n = 1$ sample), in which some domains seem more mineralized with a higher contrast (yellow dot versus star), as the section is not stained. **d**, SEM coupled with energy-dispersive X-ray spectroscopy microanalysis ($n = 1$ sample). The elemental mapping of the area shows the presence of carbon (C in red), calcium (Ca in purple) and phosphorus (P in turquoise) and confirms that the Ca and P are more pronounced in the granular (yellow dot) part of the matrix than in the fibrillar part (yellow star).

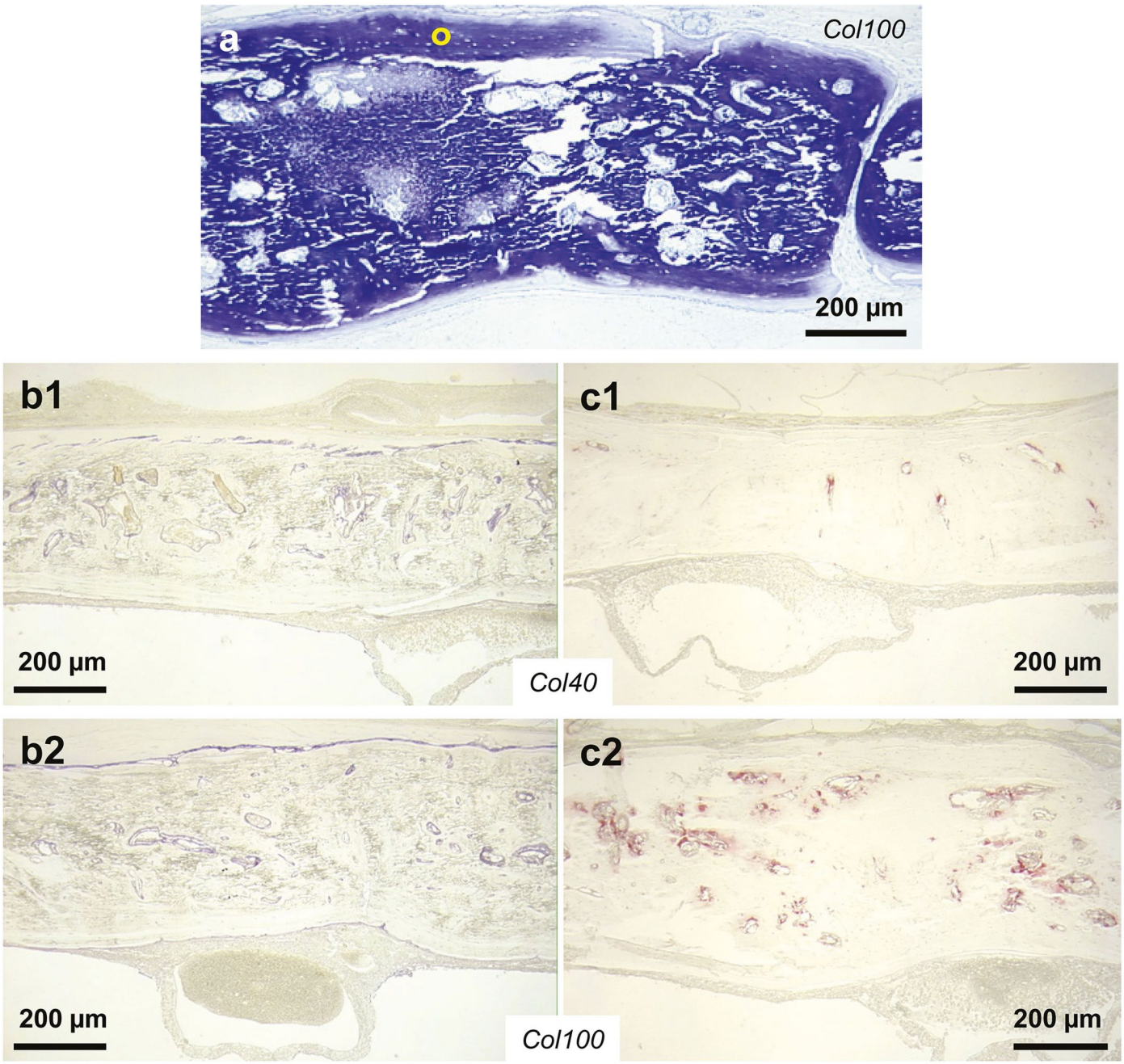

Extended Data Fig. 5 | Toluidine blue, ALP and TRAP stains for rat experiments. a, Col100 histological thin sections stained with toluidine blue (n = 9 defects) show the formation of lamellar bone on the external surface of the matrix (yellow circle). **b**, ALP detection sections (n = 10 and 9 for Col40 and Col00, respectively). A thin layer of ALP-positive cells (osteoblasts) lines at the exocranial surface and numerous cells are observed in the mineralized formations for both Col40 (**b1**) and Col100 (**b2**). **c**, TRAP detection sections (n = 10 and 9 for Col40 and Col00, respectively). Few TRAP-positive cells (osteoclasts) are found in Col40 (**c1**; around 4 osteoclasts mm^{-1}), whereas many osteoclasts (around 7 osteoclasts mm^{-1}) are homogeneously distributed within the newly formed bone tissue in Col100 (**c2**).

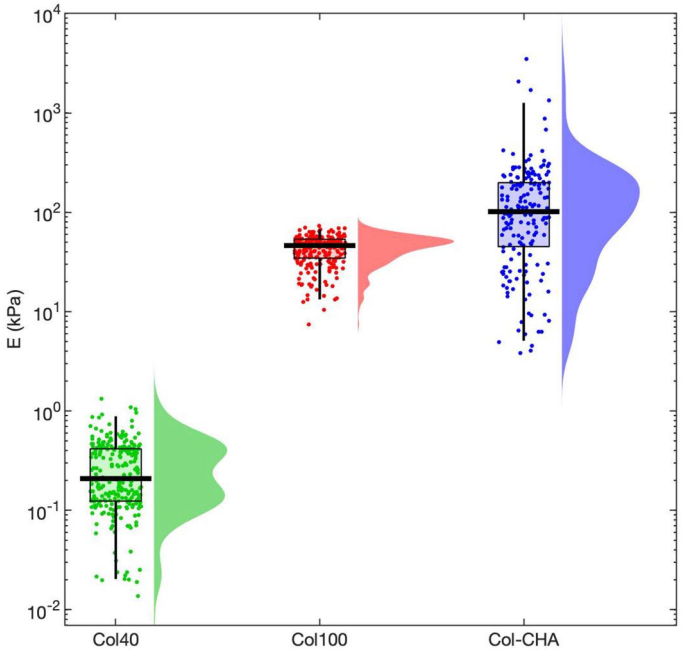

Extended Data Fig. 6 | Mechanical characterization of the Col40, Col100 and Col-CHA matrices. Distributions of the local Young's modulus *E* inferred from typically 200 independent indentation tests performed on the Col40 matrix (left, $n = 265$ independent microindentations), the Col100 matrix (centre, $n = 230$ independent microindentations) and the Col-CHA matrix (right, $n = 183$ independent microindentations). The minimum and maximum of the whiskers respectively correspond to cumulative probabilities of 0.02 and 0.98, whereas the bounds of the box indicate the first and third quartiles and the centre of the box shows the median. The probability density shown with a shaded area is that of the logarithm of the effective Young's modulus. See also Supplementary Table 1.

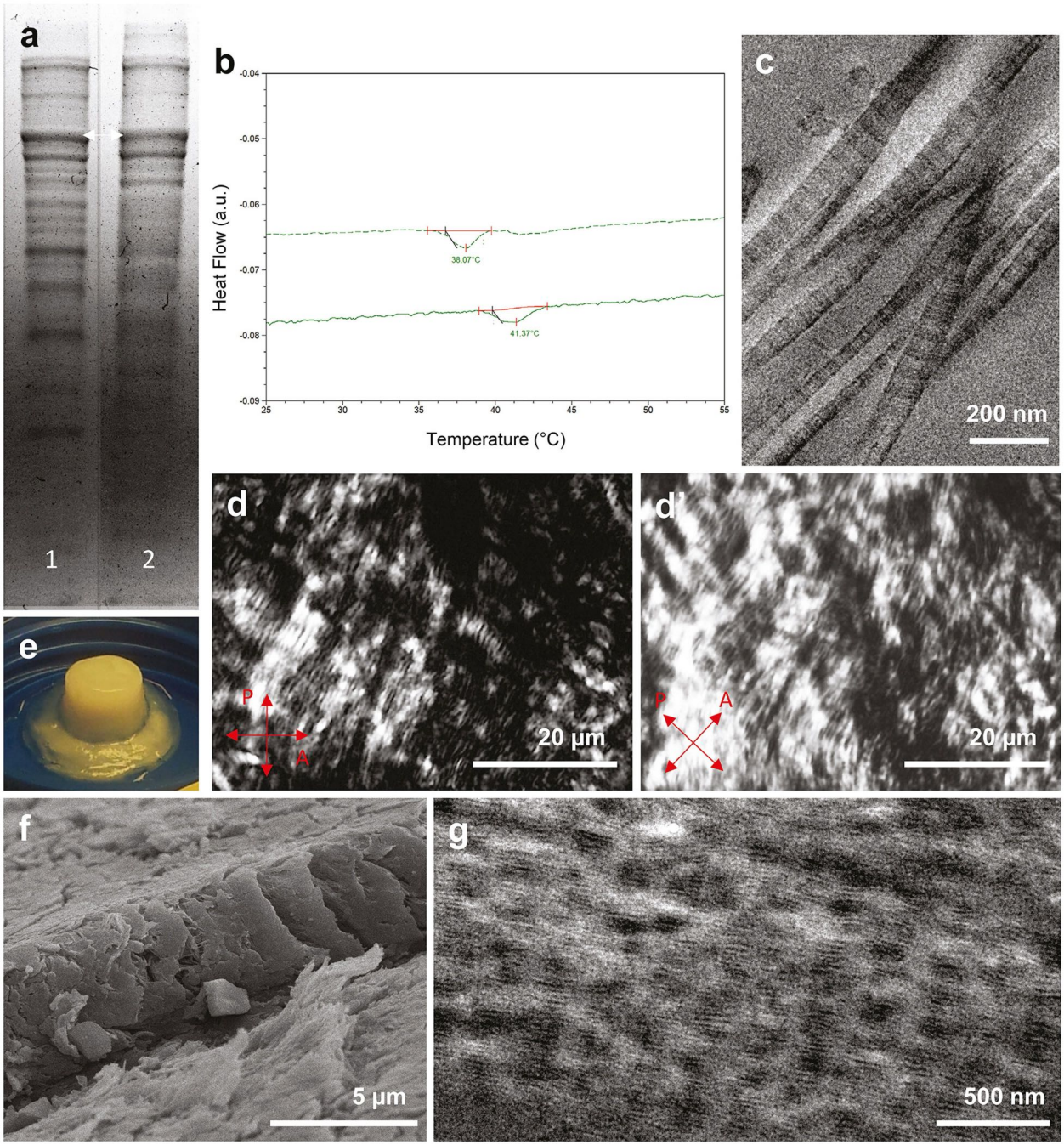

Extended Data Fig. 7 | Comparison between rat tail collagen and clinical-grade collagen. a, SDS-PAGE of type I collagen extracted from rat tails tendons (1, $n = 1$ sample) and bovine dermis (commercialized by Symatese as clinical grade) (2, $n = 1$ sample), which confirms the higher purity of the commercial solution. The white double-headed arrow shows the band corresponding to the α chain of type I collagen (125.103 KDa). **b**, Differential scanning calorimetry of a collagen solution extracted from rat tail tendons (dashed line, 7 mg ml^{-1}) and from bovine dermis (clinical grade) (solid line, 5 mg ml^{-1}). The endothermic peak is seen at temperature around 40 °C and is typical of collagen denaturation into gelatine that occurs through the irreversible unfolding of the triple helix (ref. 57). The purest collagen solution is the most stable, which may be because of a higher number of interactions between molecules. **c**, TEM observations of an ultrathin section of clinical-grade collagen fibrils showing the typical cross-striated pattern ($n = 3$ samples). **d**,**d'**, Polarized light microscopy of clinical-grade collagen solution (concentration approximately 80 mg ml^{-1}) observed between crossed polars (at 0° (**d**) and at 45° (**d'**)) and showing the typical birefringence of cholesteric order (alternating bright and dark bands). **e**, Picture of a ColCG-CHA matrix. **f**, SEM micrograph of a ColCG-CHA matrix ($n = 1$ sample) showing a periodic stratification typical of the twisted plywood organization. **g**, TEM micrograph of a ColCG-CHA matrix ($n = 1$ sample) showing the co-alignment between apatite platelets and the main axis of collagen fibrils.

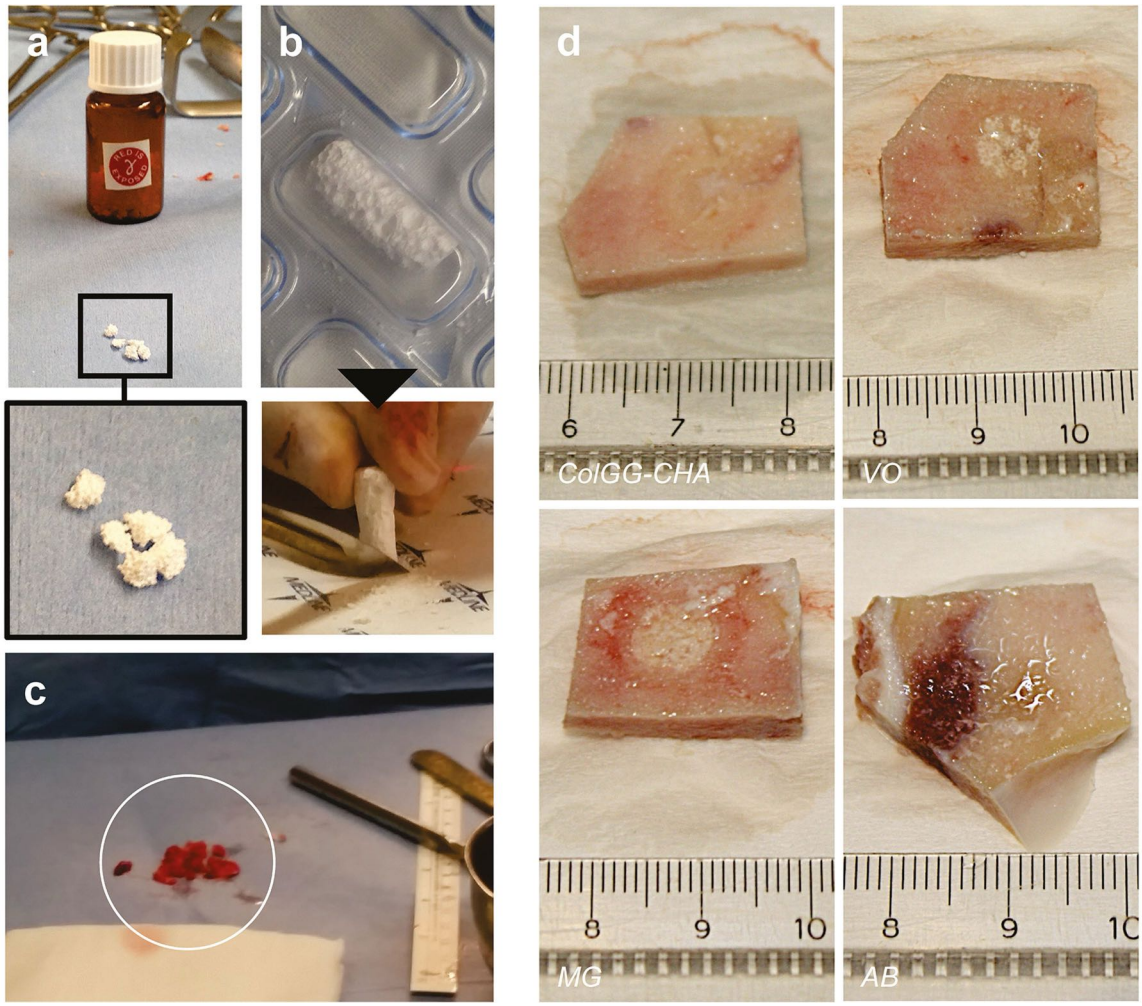

Extended Data Fig. 8 | Pictures of implanted materials and macroscopic evaluation of the bone explants (ewe study no. 2). a,**b**, Commercial ceramics biomaterials MG granules (**a**) and VO block (**b**). Granules are directly implanted into the defect, whereas ceramic blocks are first cut and then implanted to fit the defect. **c**, Bone fragments extracted from the iliac crest used as bone filler, that is, AB graft. **d**, ColCG-CHA biomimetic material, MG, VO and AB explants. The remaining white ceramic material is seen on the VO and MG ceramics-implanted explants.

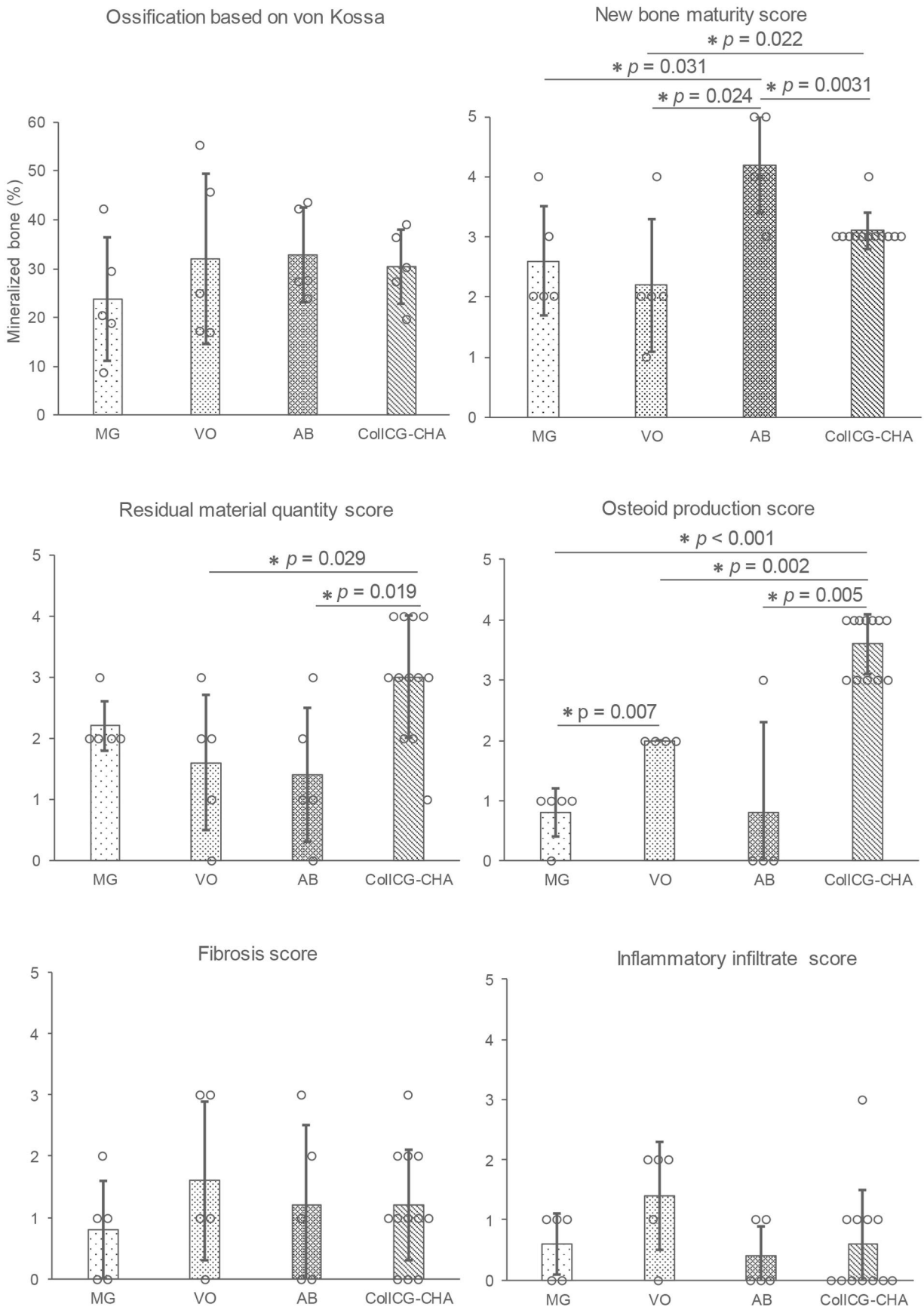

Extended Data Fig. 9 | See next page for caption.

Extended Data Fig. 9 | Histopathological scoring for the four implanted materials (ewe study no. 2). ColCG-CHA, MG, VO and AB. Blinded histopathological scoring data were analysed from the total number of animals included in each group, as indicated in the bars (n = 12 for ColCG-CHA and n = 5 MG, VO and AB, respectively, except for von Kossa, in which n = 5 defects for all groups, and for osteoid production score, in which n = 4 for VO and AB). Data were expressed as mean ± s.d. and compared using nonparametric Kruskal–Wallis with two-sided Mann–Whitney multiple comparison test. *Significant difference with $P < 0.05$.

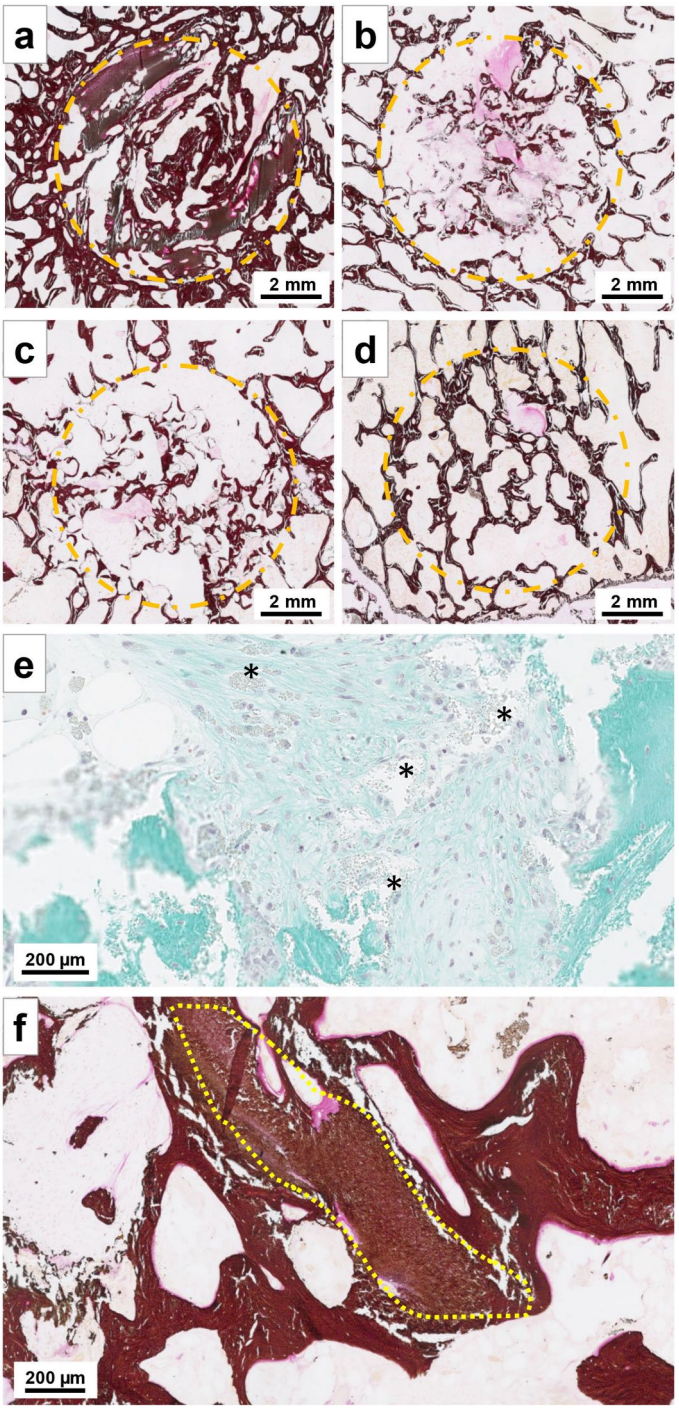

Extended Data Fig. 10 | Histological evaluation for no. 2 ewe experiment. **a**–**d**, Histological thin sections stained with von Kossa for ewe bone defect implanted with ColCG-CHA (**a**), MG (**b**), VO (**c**) and AB (**d**) ($n = 5$ defects for all groups). The dashed yellow circle represents the approximate initial defect (8 mm diameter). **e**, Histological thin section stained with GT of MG ($n = 5$ defects) implantation site showing black precipitates residues of the ceramic biomaterial (stars), either free or phagocytized by macrophages. **f**, The von Kossa staining highlights the in situ mineralization of ColCG-CHA (highlighted within the dashed yellow line).

nature portfolio

Corresponding author(s): Nadine NASSIF

Last updated by author(s): Sep 20, 2024

Reporting Summary

Nature Portfolio wishes to improve the reproducibility of the work that we publish. This form provides structure for consistency and transparency in reporting. For further information on Nature Portfolio policies, see our Editorial Policies and the Editorial Policy Checklist.

Statistics

For all statistical analyses, confirm that the following items are present in the figure legend, table legend, main text, or Methods section.

n/a	Confirmed	
☐	☒	The exact sample size (*n*) for each experimental group/condition, given as a discrete number and unit of measurement
☐	☒	A statement on whether measurements were taken from distinct samples or whether the same sample was measured repeatedly
☐	☒	The statistical test(s) used AND whether they are one- or two-sided *Only common tests should be described solely by name; describe more complex techniques in the Methods section.*
☒	☐	A description of all covariates tested
☒	☐	A description of any assumptions or corrections, such as tests of normality and adjustment for multiple comparisons
☐	☒	A full description of the statistical parameters including central tendency (e.g. means) or other basic estimates (e.g. regression coefficient) AND variation (e.g. standard deviation) or associated estimates of uncertainty (e.g. confidence intervals)
☐	☒	For null hypothesis testing, the test statistic (e.g. *F*, *t*, *r*) with confidence intervals, effect sizes, degrees of freedom and *P* value noted *Give P values as exact values whenever suitable.*
☒	☐	For Bayesian analysis, information on the choice of priors and Markov chain Monte Carlo settings
☒	☐	For hierarchical and complex designs, identification of the appropriate level for tests and full reporting of outcomes
☒	☐	Estimates of effect sizes (e.g. Cohen's *d*, Pearson's *r*), indicating how they were calculated

Our web collection on statistics for biologists contains articles on many of the points above.

Software and code

Policy information about availability of computer code

Data collection	DataViewer V2 (Optics 11) Faxitron SR v1.5
Data analysis	MATLAB (release R2018B) software for mechanical characterization analysis NDP.view2.8.24 for ewe histological viewing RadiAnt DICOM Viewer 2022.1.1 Excel v16.89.1 for basic statistics and plotting ImageJ v1.52a software (Fiji, Tokyo, Japan) was used to analyse radiographic images from the rat experiment as well as scans and radio images (Faxitron) from the first ewe experiment in order to estimate the percentage of bone filling ImageJ2 v2.0.0 software (Fiji, Tokyo, Japan) for ewe (n°2 experiment) histomorphometric analysis WAXD data was integrated radially using FIT2D version 18 (beta) software NRecon Skyscan Software 1.7.1.6. (Bruker) for 3D reconstruction

For manuscripts utilizing custom algorithms or software that are central to the research but not yet described in published literature, software must be made available to editors and reviewers. We strongly encourage code deposition in a community repository (e.g. GitHub). See the Nature Portfolio guidelines for submitting code & software for further information.

Data

Policy information about availability of data

All manuscripts must include a data availability statement. This statement should provide the following information, where applicable:

- Accession codes, unique identifiers, or web links for publicly available datasets
- A description of any restrictions on data availability
- For clinical datasets or third party data, please ensure that the statement adheres to our policy

All data generated or analysed during this study are included in the manuscript (and the supplementary information files) or available upon request to the corresponding author (apply to raw imaging data for all samples).

Research involving human participants, their data, or biological material

Policy information about studies with human participants or human data. See also policy information about sex, gender (identity/presentation), and sexual orientation and race, ethnicity and racism.

Reporting on sex and gender	N/A
Reporting on race, ethnicity, or other socially relevant groupings	N/A
Population characteristics	N/A
Recruitment	N/A
Ethics oversight	N/A

Note that full information on the approval of the study protocol must also be provided in the manuscript.

Field-specific reporting

Please select the one below that is the best fit for your research. If you are not sure, read the appropriate sections before making your selection.

☒ Life sciences ☐ Behavioural & social sciences ☐ Ecological, evolutionary & environmental sciences

For a reference copy of the document with all sections, see nature.com/documents/nr-reporting-summary-flat.pdf

Life sciences study design

All studies must disclose on these points even when the disclosure is negative.

Sample size	Rat experiment (n=10 for implant group, n= 8 for negative control group): The initial sample size was not predetermined using statistical methods but is based on previous similar work (Vigier et al. 2011) and on the maximum number of available animals regarding ethical matters, ensuring that each group (negative control, Col40 and Col100) is sufficiently represented. Considering the variability of the in vivo response, the sample size should be the maximum possible. However, considering ethical concerns, the number of animals was limited to the minimum sample size required to address the study's hypothesis. Hence, a sample size of 10 is likely to obtain tendencies between the implant group while a sample size of 8 for the negative control group (critical size defect) is sufficient as the critical size character is well-documented for 8 mm defect in rat. For ewe studies: Considering the animal used (ewe) and taking into account ethical matters, the number of animals had to be reduced to the minimum acceptable number. Thanks to the model used (Nuss et al. 2006), several implantation sites were available on each animal (a maximum of 8 by animal), allowing for a sample size of n=5 to n=12 for the groups in the two ewe experiments.
Data exclusions	Rat experiment: Animals were excluded if (i) they died during the course of the study or (ii) the surgical procedure was not performed properly (leading to inconsistent or biased bone reconstruction). Three (3) animals were excluded from the analysis. In the negative control group, one animal died during the procedure and another had an incomplete defect created during the surgcial procedure leading to an abnormal full defect reconstruction (critical size defects do not spontaneously heal). In the Col100 group, one rat had its underlying dura mater and mid-sagittal sinus severly damaged resulting in a defectuous bone reconstruction. Ewe experiments: no data were excluded. As explained in the manuscript, only the most inner part of the defect was analyzed in histology to avoid the strong and non-specific surface reaction due to the mechanical load applied on the external part.
Replication	Reproducibility was ensured by the selected sample size and by the use of well-known bone defect models, producing consistent results.
Randomization	Animals were randomly assigned to experimental groups without selection. All animals were similar in terms of species, outbreed, age and average weight.

Blinding	Rat experiment: blinding was applied for the bone percentage analysis on microradiographies. However, full blinding was not reallistic due to the presence of critical-size defect negative control (no reconstruction), and no blinding was used for the histological analysis as this analysis is more qualitative and necessarily implies several layers of material selection. N°1 ewe experiment: blinding was applied for the determination of the percentage of bone reconstruction based on scanner and radiographic images. However, full blinding was not reallistic due to the presence of critical-size defect negative control (no reconstruction), and no blinding was applied for the histological analysis. N°2 ewe experiment: blinding was applied for the comparative anatomopathological analysis (histological analysis).

Reporting for specific materials, systems and methods

We require information from authors about some types of materials, experimental systems and methods used in many studies. Here, indicate whether each material, system or method listed is relevant to your study. If you are not sure if a list item applies to your research, read the appropriate section before selecting a response.

Materials & experimental systems

n/a	Involved in the study
☒	☐ Antibodies
☒	☐ Eukaryotic cell lines
☒	☐ Palaeontology and archaeology
☐	☒ Animals and other organisms
☒	☐ Clinical data
☒	☐ Dual use research of concern
☒	☐ Plants

Methods

n/a	Involved in the study
☒	☐ ChIP-seq
☒	☐ Flow cytometry
☒	☐ MRI-based neuroimaging

Animals and other research organisms

Policy information about studies involving animals; ARRIVE guidelines recommended for reporting animal research, and Sex and Gender in Research

Laboratory animals	Two-year-old healthy French ewes (bone was extracted from the proximal part of the diaphysis and distal epiphysis of humerus and femur) 8-week-old male Wistar rats (bone was extracted from the center of calvaria)
Wild animals	The study did not involve wild animals
Reporting on sex	The findings do not apply only to one sex
Field-collected samples	The study did not involve samples collected from the field
Ethics oversight	Studies with ewes were reviewed and approved by the IMM Recherche's Institutional Animal Care and Use committee (IACUC) prior to the initiation of this study. The Animal Care and Use Committee of IMMR is registered at the CNREEA under the Ethics Committee n°37. The animal research center (IMM-Recherche) received an agreement (n°75-14-01) by the "Direction Départementale de la Protection des Populations". The studies were also performed in compliance with the Principles of Laboratory Animal Care, formulated by the National Society for Medical Research, and the Guide for the Care and Use of Laboratory Animals, by the Institute of Laboratory Animal Resources (published by the National Academy Press, Washington, D.C, 1996), as amended by the Animal Welfare Act of 1970 (P.L 91-579) and the 1976 amendments to the Animal Welfare were followed. The study with rats was reviewed and approved by the Animal Care Committee of the University Paris Descartes (No. P2.JLS.174.10).

Note that full information on the approval of the study protocol must also be provided in the manuscript.

Plants

Seed stocks	*Report on the source of all seed stocks or other plant material used. If applicable, state the seed stock centre and catalogue number. If plant specimens were collected from the field, describe the collection location, date and sampling procedures.*
Novel plant genotypes	*Describe the methods by which all novel plant genotypes were produced. This includes those generated by transgenic approaches, gene editing, chemical/radiation-based mutagenesis and hybridization. For transgenic lines, describe the transformation method, the number of independent lines analyzed and the generation upon which experiments were performed. For gene-edited lines, describe the editor used, the endogenous sequence targeted for editing, the targeting guide RNA sequence (if applicable) and how the editor was applied.*
Authentication	*Describe any authentication procedures for each seed stock used or novel genotype generated. Describe any experiments used to assess the effect of a mutation and, where applicable, how potential secondary effects (e.g. second site T-DNA insertions, mosiacism, off-target gene editing) were examined.*